energies

MDPI

Article

An Ab Initio RRKM-Based Master Equation Study for Kinetics of OH-Initiated Oxidation of 2-Methyltetrahydrofuran and Its Implications in Kinetic Modeling

Tam V.-T. Mai [1,2,†], Thanh Q. Bui [3,†], Nguyen Thi Ai Nhung [3,*], Phan Tu Quy [4], Krishna Prasad Shrestha [5,‡], Fabian Mauss [5], Binod Raj Giri [6,*] and Lam K. Huynh [7,8,*]

1 Institute of Fundamental and Applied Sciences, Duy Tan University, 06 Tran Nhat Duat, Tan Dinh Ward, District 1, Ho Chi Minh City 700000, Vietnam
2 Faculty of Natural Sciences, Duy Tan University, Da Nang City 550000, Vietnam
3 Department of Chemistry, University of Sciences, Hue University, Hue City 530000, Vietnam
4 Department of Natural Sciences & Technology, Tay Nguyen University, Buon Ma Thuot City 630000, Vietnam
5 Thermodynamics and Thermal Process Engineering, Brandenburg University of Technology, Siemens-Halske-Ring 8, 03046 Cottbus, Germany
6 Physical Science and Engineering Division, Clean Combustion Research Center, King Abdullah University of Science and Technology (KAUST), Thuwal 23955-6900, Saudi Arabia
7 School of Chemical and Environmental Engineering, International University, Quarter 6, Linh Trung Ward, Thu Duc City, Ho Chi Minh City 700000, Vietnam
8 Vietnam National University, Ho Chi Minh City 700000, Vietnam
* Correspondence: ntanhung@hueuni.edu.vn (N.T.A.N.); binod.giri@kaust.edu.sa (B.R.G.); hklam@hcmiu.edu.vn (L.K.H.); Tel.: +84-(8)-2211-4046 (ext. 3233) (L.K.H.); Fax: +84-(8)-3724-4271 (L.K.H.)
† These authors contributed equally to this work.
‡ Current address: Los Alamos National Laboratory, Los Alamos, NM 87545, USA.

Abstract: Cyclic ethers (CEs) can be promising future biofuel candidates. Most CEs possess physico-chemical and combustion indicators comparable to conventional fuels, making them suitable for internal combustion engines. This work computationally investigates the kinetic behaviors of hydrogen abstraction from 2-methyl tetrahydrofuran (2MTHF), one of the promising CEs, by hydroxyl radicals under combustion and atmospheric relevant conditions. The various reaction pathways were explored using the CCSD(T)/cc-pVTZ//M06-2X/aug-cc-pVTZ level of theory. The Rice–Ramsperger–Kassel–Marcus-based master equation (RRKM-ME) rate model, including treatments for hindered internal rotation and tunneling, was employed to describe time-dependent species profiles and pressure and temperature-dependent rate coefficients. Our kinetic model revealed that the H-abstraction proceeds via an addition-elimination mechanism forming reaction complexes at both the entrance and exit channels. Eight different reaction channels yielding five radical products were located. The reaction exhibited complex kinetics yielding a U-shaped Arrhenius behavior. An unusual occurrence of negative temperature dependence was observed at low temperatures, owing to the negative barrier height for the hydrogen abstraction reaction from the C-H bond at the vicinity of the O-atom. A shift in the reaction mechanism was observed with the dominance of the abstraction at C_α-H of 2MTHF ring (causing negative-T dependence) and at CH_3 (positive-T dependence) at low and high temperatures, respectively. Interestingly, the pressure effect was observed at low temperatures, revealing the kinetic significance of the pre-reaction complex. Under atmospheric pressure, our theoretical rate coefficients showed excellent agreement with the available literature data. Our model nicely captured the negative temperature-dependent behaviors at low temperatures. Our predicted global rate coefficients can be expressed as k (T, 760 Torr) = $3.55 \times 10^{1} \times T^{-4.72} \times \exp[-340.0\ \mathrm{K}/T] + 8.21 \times 10^{-23} \times T^{3.49} \times \exp[918.8\ \mathrm{K}/T]$ (cm^3/molecule/s). Our work provides a detailed kinetic picture of the OH-initiated oxidation kinetics of 2MTHF. Hence, this information is useful for building a kinetic me chanism for methylated cyclic ethers.

Keywords: ab initio; RRKM-ME calculations; 2-methyl tetrahydrofuran; OH radicals; kinetic modeling

check for updates

Citation: Mai, T.V.-T.; Bui, T.Q.; Nhung, N.T.A.; Quy, P.T.; Shrestha, K.P.; Mauss, F.; Giri, B.R.; Huynh, L.K. An Ab Initio RRKM-Based Master Equation Study for Kinetics of OH-Initiated Oxidation of 2-Methyltetrahydrofuran and Its Implications in Kinetic Modeling. *Energies* **2023**, *16*, 3730. https://doi.org/10.3390/en16093730

Academic Editors: Bruno Zelić and Xavier Flotats

Received: 11 January 2023
Revised: 2 April 2023
Accepted: 18 April 2023
Published: 27 April 2023

1. Introduction

Over the past few years, there were many erratic weather patterns around the globe, showing that global warming is real. The continued burning of fossil fuels significantly increased the CO_2 in the atmosphere, accelerating global warming and causing severe damage to the ecosystem. The global energy demand continues to grow (1.5% per year). As the current energy portfolio stands today, fossil fuels will still dominate the energy sector fulfilling the major energy needs for some decades. Mitigating CO_2 emissions remains a great challenge. Therefore, the world needs clean, inexpensive, zero-carbon, and/or carbon-neutral alternative fuels. Fundamental studies targeting new fuel-engines optimization are required for future sustainability. Synthetic fuels, biofuels, and other new-generation fuels (e.g., nitrogen-based fuels) can help achieve carbon neutrality. Currently, the combustion community is working hard, focusing on new fuel-engine technologies for the welfare of today's human civilization. Recently, there was considerable interest in utilizing low low-carbon/or zero-carbon fuels from bio-sources or renewable energy sources for future advanced engines. Low- and zero-carbon fuels can significantly improve air quality and mitigate global warming. Following this interest, Rotavera and Taatjes [1] addressed a wide variety of complex molecular structures and functional groups (e.g., alcohols, esters, ketones, acyclic ethers, and cyclic ethers) in their review of the ongoing progress of advanced biofuels for either application into existing combustion systems or development of future ones. In particular, chain-branching kinetics is most commonly agreed as the frame mechanism of cyclic ether chemistry in combusting environments, which is thought coincidently to emit OH radicals as the product of low-temperature alkane oxidation. Regarding tetrahydrofuran and its derivatives, diverse data collected from different methods are still needed for a more in-depth understanding and a solid conclusion to be validated.

Among bio-derived fuels, cyclic ethers (CEs) can be promising future fuel candidates. A recent review article from Tran et al. [2] provided an overview of the significance of CEs as potential future fuels. Table 1 of Tran et al. [2] lists the physicochemical properties, including the combustion indicators, e.g., lower heating value (LHV), research octane number (RON), and derived cetane number (DCN) of various CEs. These values for CEs were compared with conventional fuels (gasoline and diesel) and ethanol and n-butanol to provide insights into the combustion performance of CEs. Except few, most CEs have DCN less than RON 90 fuel, indicating that these CEs possess auto-ignition resistance and that these CEs are suitable for gasoline engines. The LHV values of CEs are similar to those of conventional fuels and alcohols (see Table 1 of Tran et al. [2]). For example, 2-methyl tetrahydrofuran (2MTHF) has an LHV of 28.5 MJ/L, which is close to gasoline (31.6 MJ/L), diesel (36.1 MJ/L), and n-butanol (26.8 MJ/L). However, its RON of 86 and DCN of ~22 make it very suitable for gasoline engines but limit its potential use as an octane booster in gasoline blends. However, Rudolph and Thomas [3] reported that 2MTHF is highly suitable as an automotive fuel additive in spark ignition engines with satisfactory performance if mixed in a blend of 10% 2MTHF with gasoline. Alonso et al. [4] reported that a mix of 70% 2MTHF in gasoline could be used without engine modification. Similarly, Janssen et al. [5] reported that a blend of 70% 2MTHF with 30% di-n-butyl ether could be an optimum diesel blend. Due to the various advantages of 2MTHF, it emerged as one of the attractive future fuels. Its ease of production is highly conducive to commercialization. The cyclic ether can be produced in high yields from lignocellulosic biomass through furfural or levulinic acid via catalytic processes (see Tran et al. [2] and references cited therein). 2MTHF can also be obtained via hydrogenation of 2-methyl furan (a chemical intermediate), whose biomass-production pathway was well-established (see Hoang et al. [6]). Moreover, the exploration of inexpensive and efficient catalysts (non-noble-metal-based catalysts) looks promising for the economically viable production of furan-based fuels [7–10].

There are 16 studies dedicated to characterizing the combustion behavior of 2MTHF over T = 639–2240, p = 0.04 to 40 bar, and ϕ = 0.5 to ∞. These studies targeted ignition delay times, laminar flame speeds, and speciation data during the oxidation of 2MTHF

over a wide range of experimental conditions using various experimental techniques (see Table 16 of Tran et al. [2]). Again, a recent review article from Tran et al. [2] nicely comprehended the previous studies pertinent to 2MTHF oxidation. Two existing kinetic models from Tripathi et al. [11] and Fenard et al. [12] characterize the low- and high-temperature chemistry of 2-MTHF. Both models adopted the high-temperature sub-mechanism from Moshammer et al. [13]. Tripathi et al. [11] used a reaction analogy to tetrahydrofuran (THF) to estimate the rate coefficients for H-abstraction reactions by OH and HOO radicals. The low-temperature oxidation kinetics of 2MTHF was developed based on rate rules and reaction classes. Fenard et al. [12] used a similar approach but updated the rate coefficients for H-abstraction reactions of 2MTHF by HO_2 from the theoretical work of Chakravarty and Fernandes [14]. In addition, they employed the rate rules to deduce the hydrogen abstraction reactions of 2MTHF using the reaction analogy with methylcyclohexane [15]. Both models showed a remarkable performance in capturing the low- and high-temperature oxidation data (IDTs and speciation data) of 2-MTHF. The authors highlighted the importance of OH-initiated oxidation of 2MTHF. At low temperatures, Tripathi et al. [11] showed that OH radicals almost exclusively deplete 2MTHF.

Furthermore, they emphasized the importance of site-specific hydrogen abstraction reactions of OH radicals with 2MTHF. For example, the formation of tertiary α-2-methyl tetrahydrofuran radical (α-2MTHFyl radical) can undergo a second O_2 addition forming α-O_2QOOH; however, it does not lead to low-temperature branching. The formed α-O_2QOOH radical cannot experience internal H-isomerization reaction due to lack of an H-atom at the C_α site bearing OOH. On the contrary, the low-temperature branching is active for δ-2MTHFyl radical) as the δ-O_2QOOH) offers a hydrogen transfer reaction that eliminates the OH radical. The formation of δ-2MTHFyl radical will expedite the low-temperature oxidation kinetics of 2MTHF. See Figure 1 below for the nomenclature of the 2MTHFyl radical. There are no high-temperature studies of the OH + 2MTHF reaction. This highlights the need for theoretical studies of OH-initiated reactions of 2MTHF rationalizing the site-specific rate coefficients over a wide range of conditions.

A few studies reported the kinetics of OH + 2MTHF reaction at low temperatures. Wallington et al. [16] first conducted an experimental study using flash photolysis resonance fluorescence and relative rate techniques. The results from both techniques showed a good agreement, yielding the values of absolute rate coefficients given by $k(T) = (2.52 \pm 0.74) \times 10^{-12} \exp(650 \pm 80)/T]$ cm^3/molecule/s and $k(298\ \text{K}) = 2.2 \times 10^{-11}$ cm^3/molecule/s, respectively. These values of the rate coefficients show that OH radicals play a critical role in the atmospheric chemistry of 2MTHF. The lifetime of 2MTHF is short (ca. 12 h) under atmospheric conditions. The reactions of 2MTHF with O_3 and NO_3 radicals should result in a negligibly slow depletion of 2MTHF. Recently, the experimental work of Illés et al. [17] reinforced the earlier reports of Wallington et al. [16] for the rate coefficient of the 2MTHF + OH reaction. Illés et al. [17] used the low-pressure fast discharge flow (DF) experiments coupled with resonance fluorescence detection of OH to directly measure a rate coefficient of $k(298\ \text{K},\ 2.64\ \text{bar He}) = (1.21 \pm 0.14) \times 10^{-11}$ cm^3/molecule/s. Their additional experiments using the relative-rate/gas-chromatographic method yielded the rate coefficient $k(298\ \text{K},\ 1030\ \text{mbar air}) = (2.65 \pm 0.55) \times 10^{-11}$ cm^3/molecule/s. In a subsequent study, Illés et al. [18] measured the temperature dependence of the rate coefficients for the OH + 2MTHF reaction. Their rate expression can be given by $k(T) = (3.88 \pm 0.55) \times 10^{-12} \exp[(560.5 \pm 43.3)/T]$ cm^3/molecule/s for the temperature range of 260–360 K. The reaction of OH radicals with 2MTFH displays a negative temperature dependence at low temperatures. This unusual occurrence of a negative T-dependence of the hydrogen abstraction reaction may reveal a negative barrier height for certain reaction pathways of OH + 2MTHF. In summary, one can expect a complex kinetic behavior of the hydrogen abstraction reaction of 2MTHF by OH radicals. To our knowledge, no prior studies investigated the detailed kinetics discerning the role of each reaction channel in the OH + 2MTHF reaction.

2MTHF is not only a promising biofuel candidate but also it is present in the oxidation kinetics of hydrocarbons and oxygenates (see Tran et al. [2]). Therefore, it is critical to understand the kinetics of OH-initiated oxidation of 2MTHF as OH radical is abundant under combustion and atmospheric conditions. In addition to its importance in the atmospheric environment, the kinetic information would also help assist engine design and biofuel development. Since there is no detailed kinetic study available yet for OH + 2MTHF reaction, this work aims: (i) to fully characterize the potential energy surface for all plausible channels using high-level CCSD(T)/cc-pVTZ//M06-2X/aug-cc-pVTZ level of theory; (ii) to report the thermochemical data for 2MTHF and its radicals using atomization and isodesmic schemes based on CBS-QB3 and W1U composite methods; (iii) to use RRKM-ME code to reasonably predict the temperature and pressure dependence of the rate coefficients for each channel; (iv) to evaluate the impact of the derived rate coefficients in the kinetic modeling of 2MTHF oxidation. The thermodynamic/kinetic information, including the detailed mechanistic insights (product branching and the distribution of the intermediates/products) from this work, will facilitate the modeling and simulation of MTHF-related systems for a wide range of atmospheric and combustion applications.

2. Computational Details

All stationary points (i.e., reactants, intermediate complexes, transition states, and products) involved in the title reaction were optimized at the M06-2X/aug-cc-pVTZ level of theory [19,20] implemented in Gaussian 09 program suite [21]. The optimized structures are provided in Figure S1 of Supplementary Information (SI). For each species, the harmonic vibrational frequencies were also computed at the same level of theory. The vibrational frequencies were scaled by a factor of 0.971 [22] to account for the difference between experimental and computed data. The scaled vibrational frequencies were employed to calculate the thermodynamic parameters and rate coefficients. In addition, the intrinsic reaction coordinate (IRC) [23,24] calculations were also performed at the M06-2X/aug-cc-pVTZ level of theory, ensuring a transition state of an elementary reaction connects its corresponding reactant(s) and product(s) appropriately.

The optimized geometries, zero-point energy (ZPE), and harmonic wavenumbers, calculated at M06-2X/aug-cc-pVTZ level, for the lowest-energy lying conformer for all possible stationary points involved in the title reaction are provided in Table S1 and Figure S1 of Supplementary Information (SI). Note that the lowest-energy lying conformers for the species involved, together with the hindered internal rotation (HIR) treatment, were used for thermodynamic and kinetic analyses. Figure 1 presents the optimized structures of selected species, including the reactant (**2MTHF**), pre-reactive complexes (**RC**), transition states (**TS**), product complexes (**PC**), a free radical (**OH**), and a water molecule (**H_2O**). Figure 1 also displays the literature data for OH and H_2O [25,26] in parentheses, validating our computational method for the OH + 2MTHF chemical system. The C-H bond lengths in 2MTHF, in their most stable structural configuration, are almost identical, ranging from 1.09 to 1.10 Å.

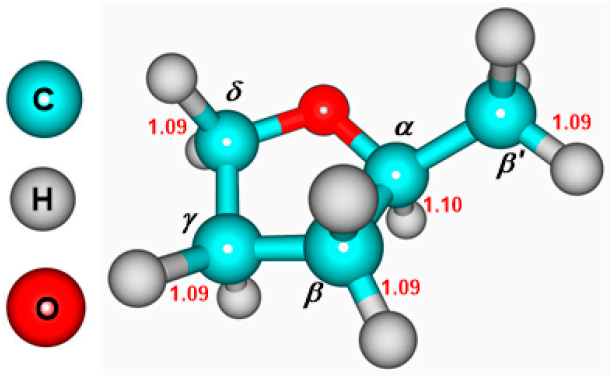

2MTHF

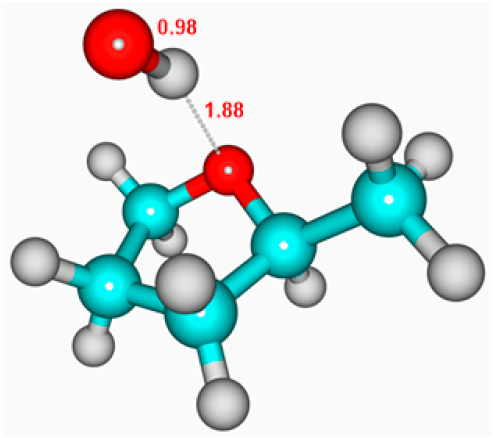

Pre-reactive complex (RC)

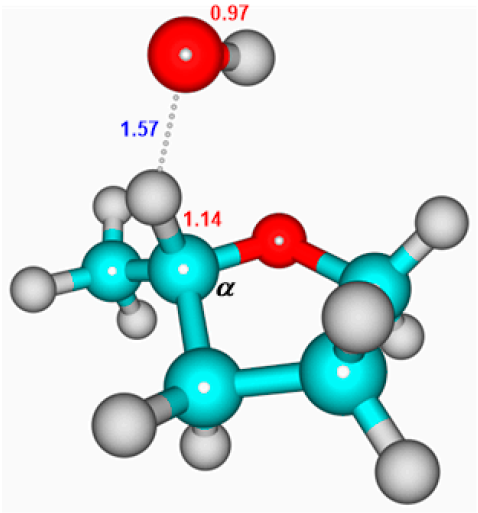

TS1 ($\nu^{\ddagger}$ = −625.8 cm^{-1})

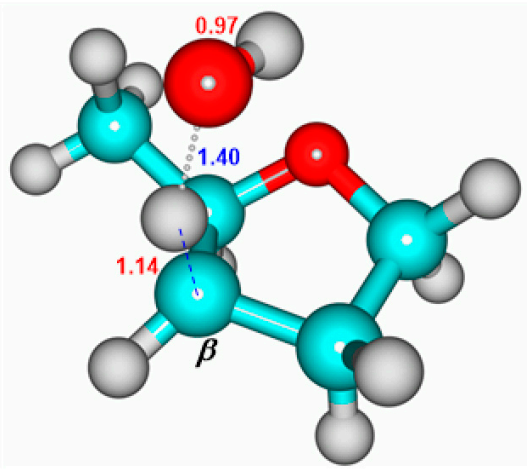

TS2a ($\nu^{\ddagger}$ = −987.6 cm^{-1})

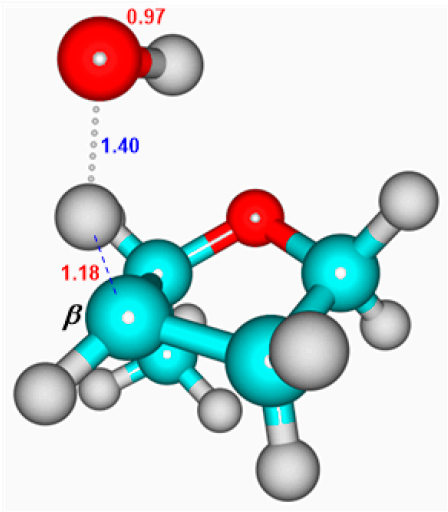

TS2b ($\nu^{\ddagger}$ = −1002.3 cm^{-1})

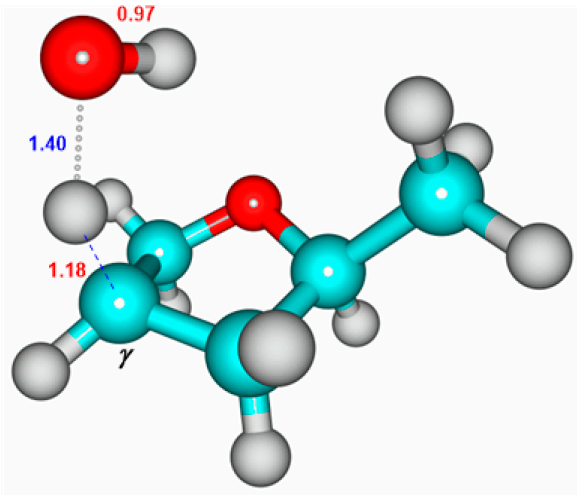

TS3a ($\nu^{\ddagger}$ = −983.3 cm^{-1})

Figure 1. *Cont.*

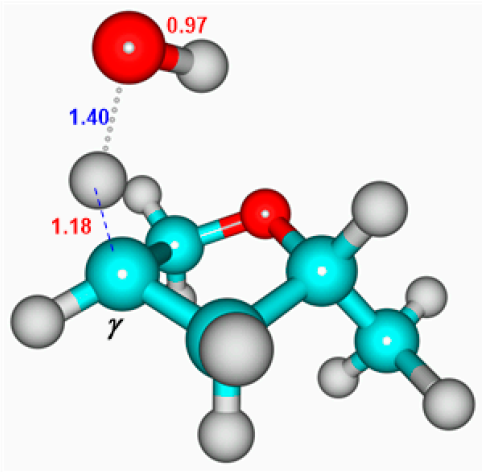

TS3b ($\nu^{\ddagger}$ = −975.8 cm^{-1})

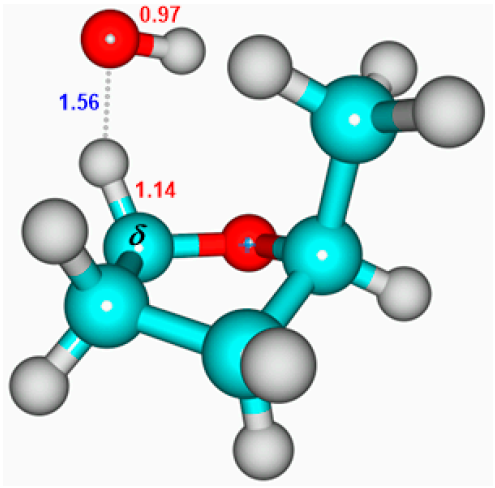

TS4a ($\nu^{\ddagger}$ = −721.9 cm^{-1})

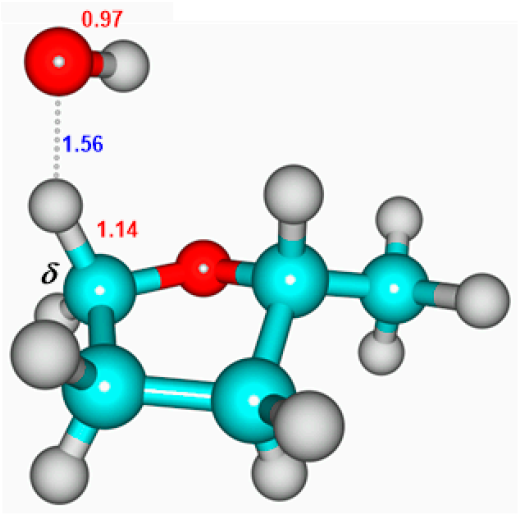

TS4b ($\nu^{\ddagger}$ = −720.2 cm^{-1})

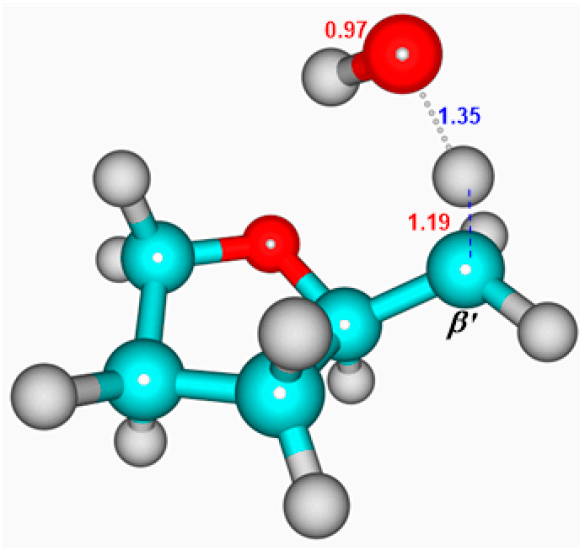

TS5 ($\nu^{\ddagger}$ = −1115.9 cm^{-1})

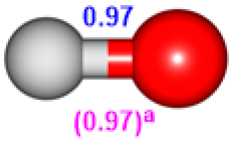

OH

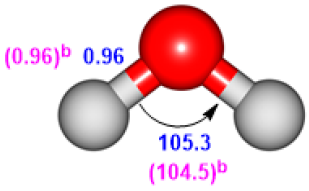

H2O

Figure 1. Optimized structures of selected species (2MTHF, RC, TSs, OH radical, and H_2O) involved in the title reaction, calculated at the M06-2X/aug-cc-pVTZ method. Only key bond lengths (Å) and bond angles (°) are provided. [a,b] Values of OH and H_2O are collected from the experimental data [26,27], respectively. "$\nu^{\ddagger}$" stands for the imaginary frequency (cm^{-1}).

Truhlar's M06 functionals are known to predict structures and frequencies for several chemical systems accurately [28,29]. Particularly, the M06-2X/aug-cc-pVTZ level is widely used to predict the rate coefficients reliably for several chemical systems, e.g., OH-initiated oxidation kinetics of imidazole [30], pyrrole [31], *trans*-decalin [32], oxazole [33], aniline [34], 1,4-cyclochexadiene [35], cyclopentadiene [36], 1,4-pentadiene [37], monoethanolamine [38],

and dipropyl thiosulfinate [39]. However, for higher accuracy, the energies of the stationary points were refined with more expensive CCSD(T)[40–42]/cc-pVTZ single-point calculations using the M06-2X/aug-cc-pVTZ optimized geometry. The quantum method employed can now be denoted as CCSD(T)/cc-pVTZ//M06-2X/aug-cc-pVTZ level of theory. The refined energies at CCSD(T)cc-pVTZ//M06-2X/aug-cc-pVTZ level of theory are also provided in Table S1. T1 diagnostics [43,44] values for the closed-shell and open-shell species were performed. All values of T1 diagnostics were less than 0.02, indicating that single-reference electron correlation methods are appropriate for 2MTHF + OH chemical system (see Table S2 of Supplementary Information (SI)).

The thermodynamic and kinetic calculations (e.g., phenomenological rate coefficients $k(T, p)$ and time-resolved species profiles) were carried out using the stochastic [45,46] Rice–Ramsperger–Kassel–Marcus-based master equation (RRKM-ME) rate model implemented in the multi-species multi-channel (*MSMC*) code [47,48]. The rigid-rotor harmonic oscillator (RRHO) model was adopted for the calculations, except for the low-torsional modes. The low-torsional vibrational modes were treated as one-dimensional hindered rotors. For CH_3 and OH rotors, the hindered internal rotation (HIR) potential energy $V(\theta)$ as a function of torsional angle (θ) was computed via relaxed potential energy scans with a step size of 10° using M06-2X/cc-pVDZ level of theory (see Figure S2 of SI). The HIR correction was implemented using the procedure described elsewhere [49]. Here, the HIR parameters were automatically generated using the MSMC graphical user interface (GUI) [50,51]. The Beyer−Swinehart algorithm [52] was adopted for the harmonic oscillator (HO) vibrational modes to calculate the density/sum of states. Then, the external/hindered rotational modes were convoluted with density/sum of states using the fast Fourier transform (FFT) approach [53]. The energy bin size of 1 cm^{-1} was chosen for the density of states (DOS) calculations. The correction for the quantum tunneling was calculated using one-dimensional asymmetrical Eckart potential [54]. The uncoupled electronic partition function of OH radical was calculated using $Q_e\,(T) = 2\,(1+ \exp(-1671.2\ J\ mol^{-1}/RT)$, where R is the universal gas constant. Due to spin-orbit coupling, the two quantum states of OH radical, $^2\Pi_{3/2}$ and $^2\Pi_{1/2}$, differ by an energy of 1671.2 J mol^{-1} = 139.7 cm^{-1} [55] and have quantum weights of 2 each. For these calculations, a large number of stochastic trials of 10^8 were used.

A single exponential collisional energy transfer model with a temperature-dependent $<\Delta E_{down}> = 250.0 \times (T/298)^{0.8}$ cm^{-1} for N_2 [32,56–59] was used. The Lennard–Jones (LJ) parameters of = 82.0 K and σ = 3.74 Å were used for N_2 [60], whereas for the 2MTHF ... OH, adduct, they were estimated as 396.0 K and 5.36 Å, respectively, based on the LJ parameters of 2-methyl furan (2MF) [61]. As shown later, the interaction of OH radicals with 2MTHF is a barrierless process, resulting in the formation of the pre-reactive or van der Waals complex (**RC**). The barrierless entrance channels (e.g., 2MTHF + OH → RC) were treated by taking the inverse laplace transform (ILT) technique [62] with the high-pressure-limit (HPL) rate constant $k^\infty\,(T)$ of 4.0×10^{-10} cm^3/molecule/s, corresponding to a T-independent value for the long-range transition state (LR-TST) [63]. In other words, the microcanonical rate constant $k\,(E)$ was calculated from the $k^\infty\,(T)$ using the ILT technique, the details of which can be found elsewhere [62]. Such treatment reasonably captured the experimental trend of the rate coefficients for the temperature and pressure dependence of the OH radical reactions with several chemical systems imidazole [30], pyrrole [31], *t*-amyl methyl ether (TAME) [56], CH_3SH [59], *trans*-decalin [32], N_2H_4 [57], oxazole [33], aniline [34], 1,4-cyclohexadiene [35], cyclopentadiene [36], and 1,4-pentadiene [37].

3. Results and Discussion

3.1. Thermochemical Properties

Figure 2 presents the bond dissociation energies (BDEs) at 298 K for each C-H bond of 2MTHF calculated at W1U and CBS-QB3 composite methods. Our calculated BDEs were compared with the averaged values suggested by Simmie [64], who obtained BDEs at CBS-QB3, CBS-APNO, and G4 levels of theory. As can be seen, our calculated BDE values at both

the W1U and CBS-QB3 levels of theory agree excellently with a deviation of 0.4 kcal/mol. They also showed good agreement with values reported by Simmie [64] with a maximum deviation of ~1.0 kcal/mol. Clearly, the presence of heteroatom "O" weakens the adjacent C-H bonds (C_α-H and C_δ-H bonds) of 2MTHF. This can be attributed to stabilizing the incipient 2-methyl-tetrahydrofuranyl (2MTHFyl) radical after the C-H bond cleavage at the adjacent carbon atom. Here, the stabilization is achieved through hyperconjugation between the non-bonding orbital of the oxygen atom and the half-occupied orbital of the carbon atom. Compared with the recommended value of BDE by Luo et al. [65] for cyclopentane (BDE = (95.6 ± 1) kcal/mol), the BDE for C_δ-H of 2MTHF is ca. 3 kcal/mole lower, revealing the stabilization of δ-2MTHFyl radical due to the hyperconjugation between the partially occupied orbital of C_δ atom and the non-bonding orbital of the oxygen atom in the radical. The C_α-H bond (BDE = 92.7 ± 0.1 kcal/mol) was further weakened by the presence of the CH_3 group, Here, the incipient α-2MTHFyl radical gains further stabilization by ~1.5 kcal/mol compared to δ-2MTHFyl radical as a result of additional hyperconjugation between the partially occupied orbital of C_α atom and neighboring σ orbital of the CH_3 group. The BDEs of remote C-H bonds (C_β-H and C_γ-H ~98 kcal/mol) of 2MTHF were significantly higher than that of the C-H bonds (C_δ-H > C_α-H) adjacent to the oxygen atom (see Figure 2). Here, the partially occupied orbital of β-2MTHFyl and γ-2MTHFyl radicals were too far from the oxygen atom to participate in hyperconjugation. Interestingly, the BDEs of C_β-H and C_γ-H bonds of 2MTHF are also higher by ~2.5 kcal/mol than that of C-H bonds cyclopentane. The trends observed here align with Simmi [64], who reported that the C-H bonds farther from the heteroatom "O" were stronger than the adjacent C-H bonds for 2MTHF and tetrahydrofuran. The methyl C-H bonds in 2MTHF were found to be the strongest, revealing the BDEs in the order of CH_2-H > C_β-H ≈ C_γ-H > C_δ-H > C_α-H.

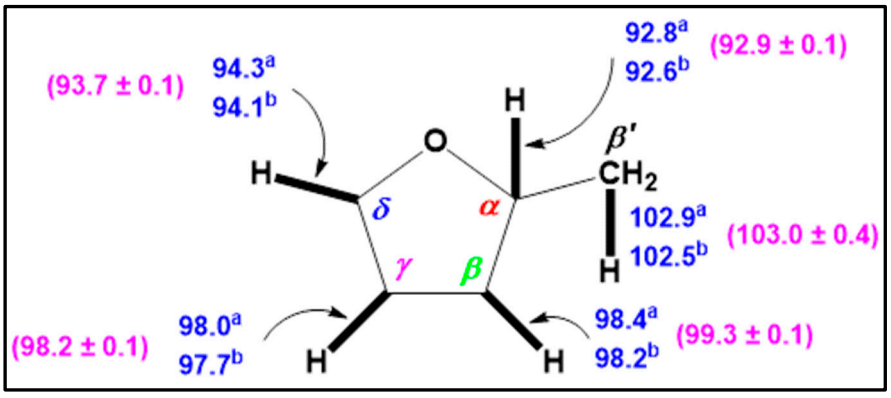

Figure 2. The C–H bond dissociation energies (BDEs) of 2MTHF at 298 K were calculated at [a] CBS-QB3 [66] and [b] W1U [67–69] methods. Units are in kcal/mol. Values in parentheses are from Simmie [64].

Our BDE analysis revealed that the oxygen atom made C_α-H and C_δ-H bonds much weaker than the other C-H bonds in 2MTHF. Based on BDEs, the former C-H bonds were expected to be more reactive with OH radicals and dominate for the OH + 2MTHF reaction, whereas CH_2-H bonds showed the least reactivity. However, such analyses are naïve and often require a detailed kinetic analysis to discern the role of hydrogen abstraction reaction at each C-H site. Usually, the reaction at each C-H site displays unique kinetics. How large a given channel contributes to the reaction depends upon several factors, e.g., enthalpy and entropy of activation, reaction path degeneracy, proper treatment of the hinder rotor partition function, and quantum tunneling.

Table 1 lists the standard enthalpy of formation ($\mathbf{\Delta_{f,298\,K}}H^\circ$) and standard molar entropy ($S^\circ_{\mathbf{298\,K}}$) for the reactants (**2MTHF** and **OH** radical) and the final products (H_2O, and the radical products: α-2MTHFyl (**P1**), β-2MTHFyl (**P2**), γ-2MTHFyl (**P3**), δ-2MTHFyl (**P4**), and 2MTHFyl (**P5**)) from various sources. Figure 3 below and Figure S1 of SI display

the structures of the product radicals. The enthalpies of formation ($\Delta_{f,298\ K}H^{\circ}$) of 2MTHF, OH, H_2O, and 2MTHFyl product radicals were computed using atomization and isodesmic schemes based on the CBS-QB3 [66] and W1U [67–69] model chemistries. Our calculated values were compared with those from Simmie [64], Auzmendi-Murua et al. [70], Wijaya et al. [71], active thermochemical tables (ATcT) [72], and NIST webbook [73]. Whenever available, we benchmarked our values against the ATcT database, which lists the most reliable internally consistent thermochemical data. As seen in Table 1, our calculated values for $\Delta_{f,298\ K}H^{\circ}$ of OH radical and H_2O using CBS-QB3 and W1U model chemistries agree remarkably with ATcT values. For example, our CBS-QB3-based value for $\Delta_{f,298\ K}H^{\circ}$ of 8.9 kcal/mol for OH radical and of −58.1 kcal/mol for H_2O agree excellently with (8.967 ± 0.006) kcal/mol and (−57.791 ± 0.006) kcal/mol ATcT values [72], respectively. In addition, our values of $\Delta_{f,298\ K}H^{\circ}$ nicely agree with the NIST database [73]. Similarly, our values of the standard molar entropy ($S^{\circ}_{298\ K}$) agree well with that listed in ATcT and NIST databases. The maximum deviation of our predicted $\Delta_{f,298\ K}H^{\circ}$ and $S^{\circ}_{298\ K}$ of OH radical and H_2O was less than 0.6 kcal/mol and 1.2 cal/mol/K, respectively, when compared to those of ATcT and NIST database; thus, our calculated values of the thermodynamic properties clearly showed a remarkable agreement with the ATcT and/or NIST database. Unfortunately, the ATcT database is not yet available for 2MTHF and its derivative radicals.

For 2MTHF and its radicals, we compared our values with that reported by Simmie [64], Auzmendi-Murua et al. [70] (both isodesmic reactions scheme-based values for $\Delta_{f,298\ K}H^{\circ}$), and that of Wijaya et al. [71] (atomization scheme based $\Delta_{f,298\ K}H^{\circ}$ value) whenever applicable (see Table 1). Our calculated values of $\Delta_{f,298\ K}H^{\circ}$ from atomization and isodesmic schemes compare remarkably with the literature data. In particular, our isodesmic values for $\Delta_{f,298\ K}H$ showed better agreement with those suggested by Simmie [64] and Auzmendi-Murua et al. [70], considering the reported uncertainties in these works. For example, our value of −53.5 ± 0.2 kcal.mol^{-1} (CBS-QB3-based value from the isodesmic scheme) and −53.4 ± 0.2 kcal.mol^{-1} (W1U-based value from the isodesmic scheme) for $\Delta_{f,298\ K}H^{\circ}$ of 2MTHF agree remarkably with the value of (−53.6 ± 0.4) kcal.mol^{-1} reported by Simmie [64] and −52.23 kcal/mol (DFT based), −53.58 (CBS-QB3 based) values reported by Auzmendi-Murua et al. [70]. Note that both groups employed isodesmic reaction schemes to obtain the values for the heat of formation of the species. Using isodesmic reaction schemes, Simmie calculated the reaction enthalpy using the three high-level composite methods, CBS-QB3, G3, and CBS-APNO, whereas Auzmendi-Murua et al. [70] used DFT-based (B3LYP with 6-31G (d, *p*) and 6-31G (2d, 2*p*) basis set) and CBS-QB3 methods. As seen in Table 1, our values of $\Delta_{f,298\ K}H^{\circ}$ also displayed similar agreements with the earlier reports for radical species. However, it is worth noting that the calculated $\Delta_{f,298\ K}H$ values from the atomization scheme using CBS-QB3, W1U model chemistries generally show marked deviations from the references. The agreement may be further improved by incorporating the spin-orbit and bond additivity corrections. In conclusion, an isodesmic scheme yields a consistent set of values for the standard enthalpy of formation.

In fact, both CBS-QB3 [66] and W1U [67–69] were used in this work to predict the thermochemical values using two approaches, atomization [74] and isodesmic-reaction [75] schemes. As seen in Table 1, at the CBS-QB3 and W1U levels, the calculated $\Delta_f H^{298\ K}$ values, using the isodesmic-reaction [75] scheme were consistent with literature values reported by Simmie et al. [64] (max. deviation of 1.3 kcal/mol for **P4**), who used the same isodesmic-reaction scheme. At the CCSD(T)/cc-pVTZ//M06-2X/aug-cc-pVTZ level, the calculated $\Delta_f H^{298\ K}$ is good for the isodesmic-reaction scheme (max deviation of 1.0 kcal/mol for **P4**) but not good for the atomization scheme (max. deviation of ~37.0 kcal/mol for 2MTHF) when compared with that of Simmie; therefore, at this level, only the isodesmic-reaction scheme should be used to obtain reliable $\Delta_f H^{298\ K}$.

Table 1. Comparison of the thermochemical properties with the literature data: Simmie [64]—isodesmic reaction schemes based on CBS-QB3, G3, and CBS-APNO methods (averaged value); Auzmendi-Murua et al. [70]—isodesmic reactions scheme based on B3LYP (bold—averaged DFT value) and CBS-QB3 (italic) methods; Wijaya et al. [71]—atomization scheme based on CBS-QB3 method; NIST = NIST webbook [73] http//:webbook.nist.gov (accessed on 1 March 2022); ATcT = Active Thermochemical Tables [72,76].

Species	Method	$\Delta_{f,298\,K}H^{\circ}$ kcal/mol	$S^{\circ}{}_{298\,K}$ cal/mol/K
2MTHF	CBS-QB3	−52.6 [a]; (−53.5 ± 0.2) [b]	79.5
	W1U	−54.7 [a]; (−53.4 ± 0.2) [b]	80.2
	CCSD(T)//M06-2X	−17.0 [a]; (−53.8 ± 0.2) [b]	81.0
	Simmie	(−53.6 ± 0.4); (−54.0 ± 0.3)	–
	Auzmendi-Murua et al.	**−52.23**, *−53.58*	80.86
	Wijaya et al.	−54.58	
OH	CBS-QB3	8.9 [a]	42.7
	W1U	8.6 [a]	42.7
	CCSD(T)//M06-2X	13.1	42.7
	ATcT	(8.967 ± 0.006)	43.9
	NIST	9.3	43.9
H_2O	CBS-QB3	−58.1 [a]	45.2
	W1U	−58.4 [a]	45.2
	CCSD(T)//M06-2X	−50.2	45.2
	ATcT	(−57.791 ± 0.006)	45.1
	NIST	−57.8	45.1
P1 (α-THFyl radical)	CBS-QB3	−11.9 [a]; (−13.2 ± 0.1) [c]	80.2
	W1U	−14.2 [a]; (−12.8 ± 0.1) [c]	80.3
	CCSD(T)//M06-2X	23.0 [a]; (−12.8 ± 0.1) [c]	80.3
	Simmie	(−13.4 ± 0.4)	–
	Auzmendi-Murua et al.	**−13.52**, *−12.51*	
P2 (β-THFyl radical)	CBS-QB3	−6.2 [a]; (−7.5 ± 0.1) [c]	81.5
	W1U	−8.6 [a]; (−7.2 ± 0.1) [c]	81.5
	CCSD(T)//M06-2X	28.0 [a]; (−7.8 ± 0.1) [c]	82.1
	Simmie 2012	(−7.0 ± 0.4)	–
	Auzmendi-Murua et al.	**−6.75**, *−7.20*	
P3 (γ-THFyl radical)	CBS-QB3	−6.7 [a]; (−8.0 ± 0.1) [c]	81.3
	W1U	−9.1 [a]; (−7.7 ± 0.1) [c]	81.4
	CCSD(T)//M06-2X	28.1 [a]; (−7.7 ± 0.1) [c]	81.7
	Simmie	(−8.1 ± 0.5)	–
	Auzmendi-Murua et al.	**−7.55**, *−6.72*	
P4 (δ-THFyl radical)	CBS-QB3	−10.4 [a]; (−11.7 ± 0.1) [c]	80.6
	W1U	−12.7 [a]; (−11.3 ± 0.1) [c]	80.8
	CCSD(T)//M06-2X	24.2 [a]; (−11.6 ± 0.1) [c]	80.1
	Simmie	(−12.6 ± 0.4)	–
	Auzmendi-Murua et al.	**−11.79**, *−11.34*	
P5 (β′-THFyl radical)	CBS-QB3	−1.8 [a]; (−3.1 ± 0.1) [c]	83.4
	W1U	−4.2 [a]; (−2.8 ± 0.1) [c]	83.6
	CCSD(T)//M06-2X	32.5 [a]; (−3.3 ± 0.1) [c]	83.5
	Simmie	(−3.3 ± 0.6)	–
	Auzmendi-Murua et al.	**−2.89**, *−2.83*	

[a] Standard enthalpy of formation ($\Delta_{f,298\,K}H^{\circ}$ in kcal/mol) using the atomization scheme based on approach CBS-QB3 and W1U model chemistries (this work). [b], [c] $\Delta_{f,298\,K}H^{\circ}$ using the isodesmic scheme (this work): CH_3OCH_3 (dimethyl ether) + $C_5H_9CH_3$ (methyl cyclopentane) → $C_5H_{12}O$ (2-methyl tetrahydrofuran) + C_3H_8 (propane) and, $[CH_2OCH_3]^{\bullet}$ (dimethyl ether radical) + $C_5H_9CH_3$ → $[C_5H_{11}O]^{\bullet}$ (2-methyl tetrahydrofuran radicals, **P1**/**P2**/**P3**/**P4**/**P5**) + C_3H_8 (propane), respectively. The experimental values for $\Delta_{f,298\,K}H^{\circ}$ are taken from NIST: CH_3OCH_3 = (−44.0 ± 0.1) [77]; $C_5H_9CH_3$ = −25.3 [78]; C_3H_8 = (−25.0 ± 0.1) [79] kcal/mol; and from the ATcT [72]: $[CH_2OCH_3]^{\bullet}$ = 0.2 kcal/mol.

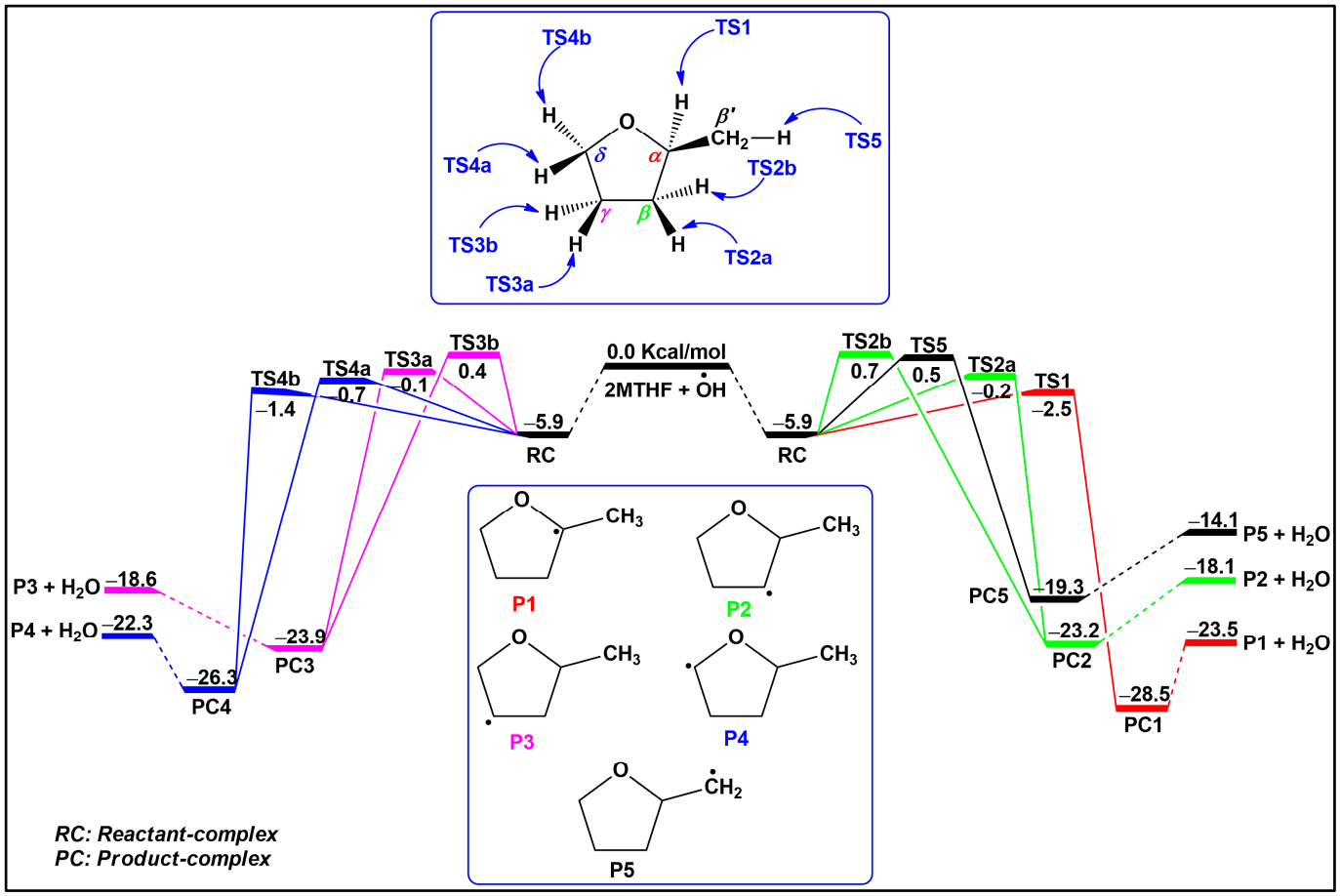

Figure 3. Potential energy profile at 0 K (+ZPE corrections) for the reaction of 2MTHF + OH, calculated at the CCSD(T)/cc-pVTZ//M06-2X/aug-cc-pVTZ level. Units are in kcal/mol.

3.2. Potential Energy Surface (PES)

As seen in Figure 1, the most stable 2MTHF was a bent conformer with the C1 point group. This results in the non-equivalence of all the ring hydrogen atoms of 2MTHF. That being said, except for the methyl hydrogen atoms, each hydrogen atom in 2MTHF is unique. Consequently, 2MTHF offers several reaction pathways with OH radicals in its potential energy surface (PES). The reaction pathways in the PES of the OH + 2MTFH reaction were extensively mapped out using the CCSD(T)/cc-pVTZ//M06-2X/aug-cc-pVTZ level of theory. The computed PES are depicted in Figure 3. The topology of the PES is similar to that seen for several OH + oxygenates reactions [80–86]. Not surprisingly, each OH + 2MTHF reaction channel has multiple steps undergoing an addition-elimination mechanism in an overall exothermic process.

As in other OH + oxygenates chemical systems, the first step involves the attractive interaction between the OH radical and 2MTHF, forming a hydrogen-bonded pre-reaction complex (**RC**). The interaction of the H atom of OH radical with the O atom of 2MTHF lowers the energy of the isolated reactants (OH + 2MTHF) by 5.9 kcal/mol. This stabilization energy of 5.9 kcal/mol for the RC (OH ... 2MTHF) is nearly identical to the hydrogen-bonded pre-reaction complex of OH + tetrahydrofuran [80,81], OH + 2,5-dimethyltetrahydrofuran [64], and OH + ethyl propyl ether [83]. In addition, Galano and Alvarez-idaboy [86] tabulate similar stabilization energies in the range of 3.1 to 7.4 kcal/mol for several pre-reaction complexes of OH + oxygenated volatile organic compounds. The RC encountered here is an example of a normal hydrogen-bonded complex with the H ... O bond length of 1.88 Å and the O-H ... O bond angle of 151°. Since the RC sits at a shallow well in the PES, it may be kinetically irrelevant under combustion-relevant

conditions. However, their life span can be long at low temperatures to affect their kinetics. Recently, Shannon et al. [84] and Gao et al. [85] highlighted the importance of such pre-reaction complexes (**RC**) at ultralow temperatures. With the inclusion of the RC in the theoretical model, the authors could describe the experimentally observed unusually high rate coefficients for the reaction of OH radicals with CH_3OH at ultralow temperatures. Galano and Alvarez-Idaboy [86] reviewed the importance of OH-bound complexes in the bimolecular reactions of OH radicals. In conclusion, **RC** can be critical in accurately describing the OH-initiated oxidation kinetics of oxygenated volatile organic compounds.

Our calculations revealed eight reaction pathways from the common RC well (see Figure 3). Our IRC calculations identified five post-reaction complexes (**PC**s) at the exit well, each corresponding to a given C-H site of 2MTHF. The formation of PCs was highly exothermic, and their relative energies were close to the dissociated final products. For example, the relative energy of **PC1** was −28.1 kcal/mol, which is close to **P1** + H_2O ($\Delta_{rxn,\,0K}H^\circ$ = −23.5 kcal/mol). As a result, they were kinetically irrelevant, and one can exclude the **PC**s in the ME kinetic model.

We observed a nice consistency of Evans–Polanyi correlation of barrier heights ($\Delta E_0^{\neq}$) with the bond dissociation energies (BDEs) and reaction enthalpies ($\Delta_{rxn,\,0K}H^\circ$). For example, the lowest-lying transition state (**TS1**) had a negative barrier height of $\Delta E_0^{\neq}$ = −2.5 kcal/mol. **TS1** corresponded to the C_α-H hydrogen abstraction, for which the BDE was the least (~92.7 kcal/mol) and reaction exothermicity ($\Delta_{rxn,\,0K}H^\circ$ = −23.1 kcal/mol) was the highest. $C_{\beta'}$-H hydrogen abstraction reaction occurred via TS5, surmounting a positive barrier height of 0.5 kcal/mol with the least overall reaction exothermicity of $\Delta_{rxn,\,0K}H^\circ$ = −14.1 kcal/mol. Note that the BDE of $C_{\beta'}$-H hydrogen was ~103 kcal/mol—the strongest C-H bond in 2MTHF. According to the Evans–Polanyi correlation, one expects **TS5** to have the highest barrier height of all channels. However, the barrier height of **TS5** ($\Delta E_0^{\ddagger}$ = 0.5 kcal/mol) was somewhat lower than TS2b ($\Delta E_0^{\ddagger}$ = 0.7 kcal/mol), owing to the extent of hydrogen bonding in the transition state. As can be seen in Figure 1, the TS5 has a "strongly bent" hydrogen bonding with the bond length ($r_{H\ldots O}$ = 2.23 Å) and the bond angle ($\delta_{O\text{-}H\ldots O}$ = 127.6°) as opposed to $r_{H\ldots O}$ = 2.32 Å and $\delta_{O\text{-}H\ldots O}$=129.7° of TS2b. Clearly, the effect of hydrogen bonding in TS5 is stronger than in TS2b, resulting in a lowering of the barrier height of TS5. There are some key features of the TSs for OH + 2MTFH reaction: (i) the breaking C-H bonds of all TSs are marginally stretched ($r_{C\ldots H}$ ranges from 1.14 Å to 1.19 Å) from 2MTHF ($r_{C\ldots H}$ ~1.09 Å), whereas the forming $r_{H\ldots O}$ ranges from 1.40 Å to 1.57 Å. The ratio of $r_{C\ldots H}$ to $r_{H\ldots O}$ ($L = r_{C\ldots H}/r_{H\ldots O}$) ranges from 0.72 to 0.88. If the L value is less than 1, the TS possesses the reactant-like character, considered as an early TS. Such reactions are expected to be exothermic, according to Hammond's postulate. Among the TSs, the structure of TS1 is closer to the reactants' geometry; therefore, this reaction has the highest exothermicity of OH + 2MTHF reaction. (ii) The barrier heights for a given C-H differ. For instance, the barrier heights for **TS4a** and **TS4b** were −0.7 and −1.4 kcal/mol, respectively, compared to those of 2-hydroxytetrahydrofuran (2OHTHF) + OH reaction [87] of −1.2 and −2.8 kcal/mol, respectively, and both lack hydrogen bonding ($r_{H\ldots O}$ > 2.64 Å). (iii) For a given C-H site, the two TSs, e.g., TS3a and TS3b, are syn- and anti-structures concerning the ring O atom of 2MTHF. The syn-form of the TS has a lower barrier than the anti-form. (iv) The reaction leading to P1 + H_2O via TS1 with the highest exothermicity ($\Delta_{rxn,\,0K}H^\circ$ = −23.5 kcal/mol) and lowest reaction barrier ($\Delta E_0^{\ddagger}$ = −2.5 kcal/mol) which is relatively lower than that of the 2OHTHF + OH reaction ($\Delta E_0^{\ddagger}$ = −1.1 kcal/mol) [87] appears to be thermodynamically and kinetically favorable. However, the role of each channel was rationalized via detailed master equation modeling, as presented below.

3.3. Kinetic Analysis

Time-Resolved Species Profiles. A stochastic RRKM-ME model was employed to obtain the time-resolved species profiles. An example of the time-resolved species at 298 K and 760 Torr is shown in Figure 4. As expected, RC appeared early in the reaction. It built up to a steady state concentration higher than a few ppm. This indicates that pressure

stabilization of RC under those conditions is unimportant. However, the RC is expected to play a critical role under ultracold temperatures and high pressures. The results are highly consistent with the potential energy profiles displayed in Figure 3. Clearly, the main product was **P1** + H_2O, followed by **P4** + H_2O. After a few microseconds, our simulation indicates an exclusive formation of **P1** + H_2O (close to 1 in mole fraction), while the mole fraction of **P4** is one order of magnitude lower. The other products are insignificant (ca. 5×10^{-3}).

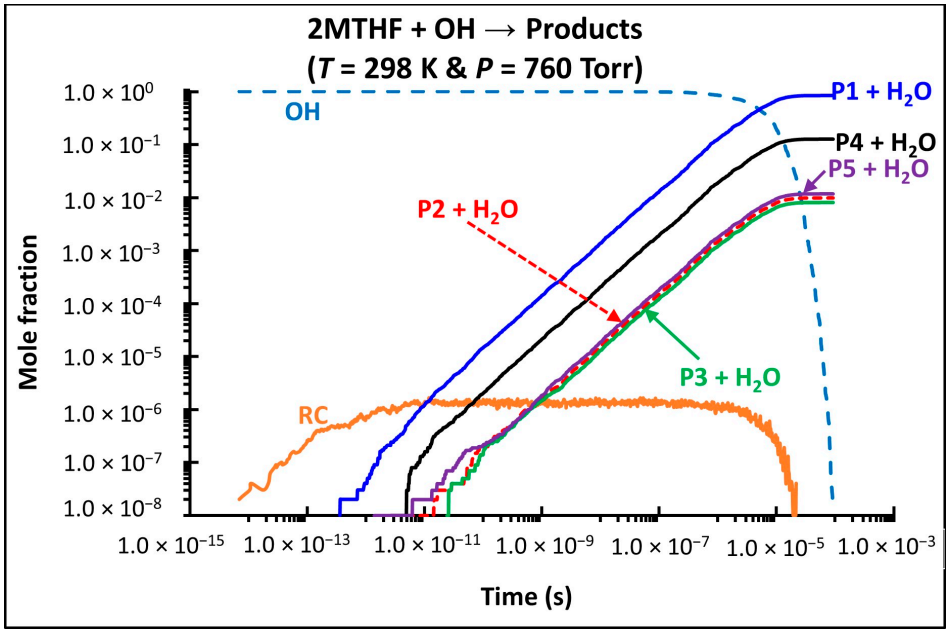

Figure 4. Time-resolved species profiles for the 2MTHF + OH → Products reaction, computed at 298 K and 760 Torr (in logarithm scale); $[2MTHF]/[N_2] = 3.0 \times 10^{-4}$, $[2MTHF]_0 >> [OH]_0$ and the number of trials = 10^8. See Figure 3 for the species notations.

Rate Coefficients k(T, p). The temperature and pressure dependence of the total rate coefficients $k_{tot}(T, p)$ for the OH + 2MTHF reaction are plotted in Figure 5 and listed in Table S3 (only from 0.76 to 7600 Torr). The fitted double-modified Arrhenius parameters for the $k_{tot}(T, p)$ are provided in Table 2 (only from 0.76 to 7600 Torr). As shown in Figure 5, the T-dependence of the rate coefficients exhibited a complex kinetic behavior, yielding a U-shaped Arrhenius behavior. At low temperatures, $k(T, p)$ showed a negative T-dependence, while they exhibited positive T-dependence at higher temperatures (e.g., beyond 670 K and at 760 Torr). The pressure dependence of the rate constants was complicated and depended on temperature due to the competition of multiple reaction pathways and the existence of the complex **RC**. The significant role of the complex **RC** is also reflected in Figure 6, where the branching ratio of the **RC** formation channel depends on both pressure and pressure, favoring low temperatures and high pressures. For the whole considered temperature range of T = 200–2000 K, the pressure effects were negligible for pressures below atmospheric. The complex kinetics of the reaction of OH radicals with 2MTHF reflects the salient features of the PES in Figure 3.

Figure 7 displays the temperature dependence of the rate coefficients for the individual channel at 760 Torr. For other pressures, they are listed in table over T = 200–2000 K. At low temperatures (T < 700 K), the hydrogen abstraction reaction via TS1 leading to **P1** + H_2O almost exclusively contributes to the total rate coefficient, while at temperatures above 700 K, the hydrogen abstraction reaction at the methyl site forming **P5** + H_2O is the dominant one. Each channel shows peculiar T-dependence, resulting in a U-shaped Arrhenius for the total rate coefficient. Owing to the negative barrier height of −2.5 kcal/mol for **TS1**, **P1** + H_2O shows a negative T-dependence. This is not the first time we encountered

an unusual negative T-dependence for the hydrogen abstraction reaction. Previously, we made similar observations for OH + 1,4-cyclohexadiene [35], OH + 1,4-pentadiene [37], and OH + 1,3,5 trimethyl benzene [88]. Interestingly, the channel **P4** + H_2O also displayed the U-shaped Arrhenius behavior. The **P2** + H_2O, **P3** + H_2O, and **P4** + H_2O channels showed similar reactivity beyond 2000 K. The **P5** + H_2O channel had positive T-dependence owing to the channel's positive barrier height of 0.5 kcal/mol. We also provided the fitted double-modified Arrhenius parameters for the $k(T, p)$ of individual channel in Table 3 (only from 0.76 to 7600 Torr).

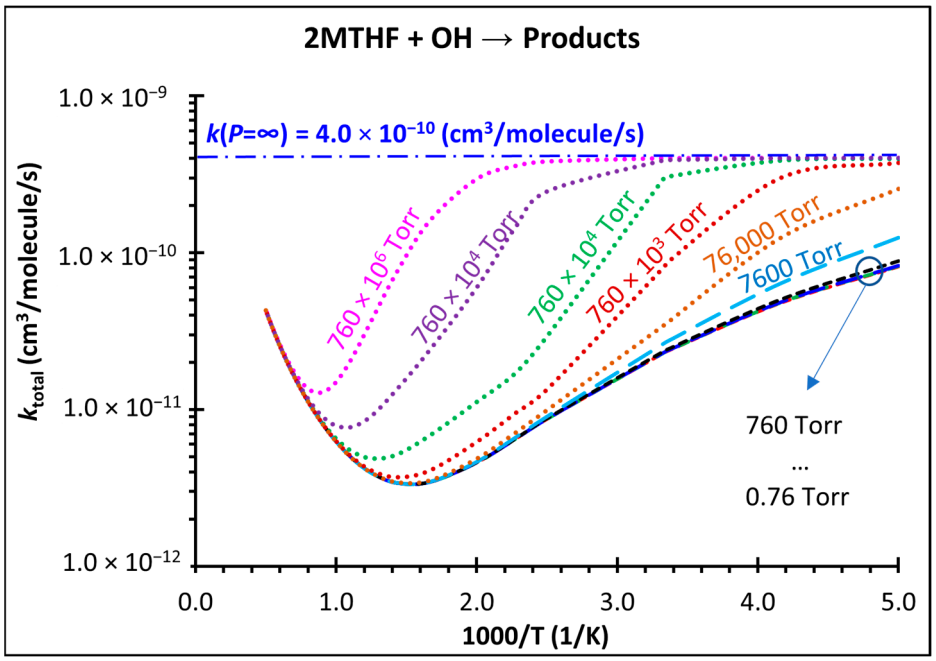

Figure 5. Temperature dependence of the calculated total rate coefficients, k_{total}, for the 2MTHF + OH → Products for various pressures from p = 0.76–760 × 10^6 Torr).

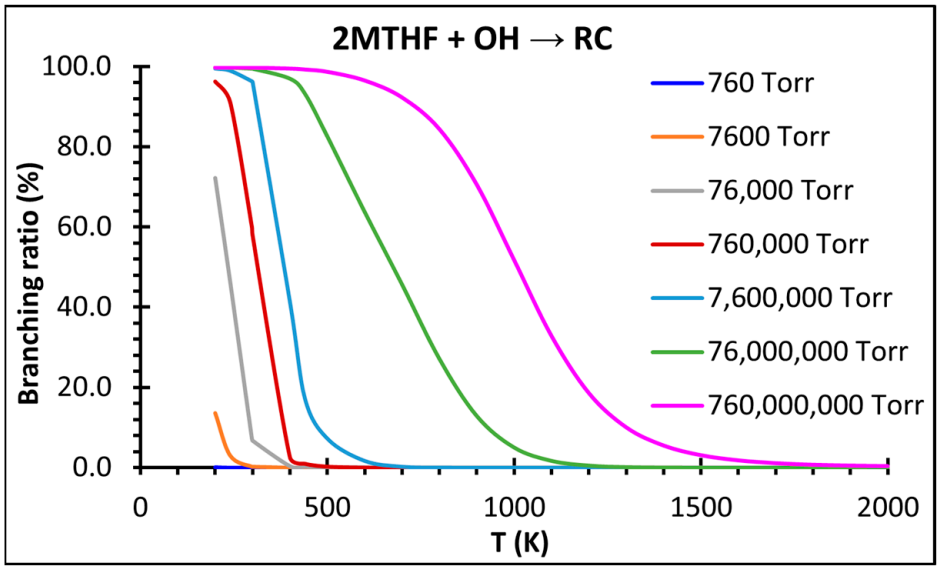

Figure 6. Temperature dependence of the branching ratio for the reaction of 2MTHF + OH → **RC** at p = 760 Torr to 760 × 10^6 Torr.

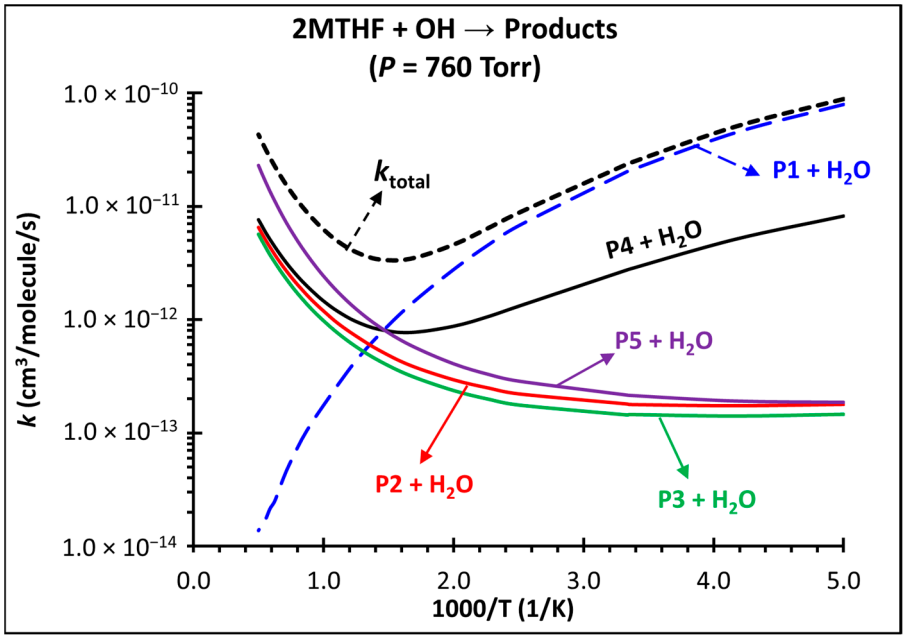

Figure 7. Calculated temperature dependence of the individual rate coefficients for the reaction of 2MTHF + OH → products at p = 760 Torr.

Table 2. The total rate coefficients, $k(T, p)$, fitted to double modified Arrhenius parameters, as given by $k(T) = A_1\ T^{n1}\ \exp\ (-E_1/T) + A_2\ T^{n2}\ \exp\ (-E_2/T)$ in units of cm^3/molecule/s for T = 200–2000 K.

p Torr	A_1 cm^3/Molecule/s	n_1	E_1 K	A_2 cm^3/Molecule/s	n_2	E_2 K	Fitting Error%
0.76	126	−4.9	418	7.1×10^{-23}	3.51	−945.2	0.7
7.6	97.2	−4.87	406.6	7.09×10^{-23}	3.51	−945.2	0.7
76	94.5	−4.86	402.2	6.88×10^{-23}	3.51	−950.7	0.7
760	35.5	−4.72	340.0	8.21×10^{-23}	3.49	−918.8	0.7
7600	1.96	−4.33	104.5	6.95×10^{-23}	3.51	−941.9	1.1

The effect of hindered internal rotation (HIR) correction is presented in Figure 8. It is evident that HIR treatment in the RRKM-ME model was crucial to predict the rate coefficients reliably. The HIR correction was significant at high temperatures, e.g., its inclusion increased the rate coefficient by a factor of 1.7 at 1000 K. However, HIR correction was insignificant over the T-range of 200 and 500 K. The tunneling correction is essential at low temperatures. At 200 K, the tunneling correction was as large as 28.9 for methyl abstraction reaction occurring via TS5. Similarly, the reaction channels via TS2a, TS2b, TS3a, and TS3b exhibited large tunneling correction. The tunneling was still significant at 300 K and increased the rate coefficients by 2 to 4. As expected, the tunneling correction was not important beyond 1000 K. The calculated Eckart tunneling factors for various temperatures are listed in Table S4 of SI.

Branching Ratios: Temperature-dependence of the product branching ratios at 760 Torr are plotted in Figure 9. **P1 +** H_2O was the primary product at low temperatures, e.g., ~85% at 200 K. However, its contribution diminished rapidly with increasing temperature. At 1000 K, the contribution of **P1 +** H_2O was almost negligible. Beyond 700 K, the **P5 +** H_2O channel became dominant. This channel contributed roughly 60% at 2000 K, nearly 3-fold higher than the **P4 +** H_2O channel. Above 700 K, the contribution of **P2 +** H_2O remained at ~18%, whereas **P3 +** H_2O contributed ~14% to the total rate coefficient. Under very high pressures, the reaction exclusively (~100%) formed RC at low temperatures ($T \leq 500$ K).

The branching ratios of the RC at various pressures and temperatures are provided in Figure S3 of Supplementary Information (SI) .

Table 3. Modified Arrhenius expressions, $k(T) = \mathrm{A} \times T^{\mathrm{n}} \times \exp(-E/T)$, for the individual channels of 2MTHF + OH → products. The unit of k and A and E and T are in cm^3/molecule/s and K, respectively. The rate expressions are valid over T = 200–2000 K.

2MTHF + OH → P1 + H_2O	
p = 0.76 Torr	$k_{P1}(T) = 3.78 \times 10^{-1} \times T^{-4.09} \times \exp(-123.2\ \mathrm{K}/T)$ (error fitting ~ 1.2%)
p = 7.6 Torr	$k_{P1}(T) = 3.31 \times 10^{-1} \times T^{-4.07} \times \exp(-115.2\ \mathrm{K}/T)$ (error fitting ~ 1.4%)
p = 76 Torr	$k_{P1}(T) = 2.88 \times 10^{-1} \times T^{-4.05} \times \exp(-104.8\ \mathrm{K}/T)$ (error fitting ~ 1.4%)
p = 760 Torr	$k_{P1}(T) = 2.53 \times 10^{-1} \times T^{-4.04} \times \exp(-83.3\ \mathrm{K}/T)$ (error fitting ~ 1.3%)
p = 7600 Torr	$k_{P1}(T) = 1.23 \times 10^{-1} \times T^{-3.95} \times \exp(14.7\ \mathrm{K}/T)$ (error fitting ~ 1.3%)
p = 76,000 Torr	$k_{P1}(T) = 9.92 \times 10^{-1} \times T^{-4.22} \times \exp(-144.5\ \mathrm{K}/T)$ (error fitting ~ 3.2%)
2MTHF + OH → P2 + H_2O	
p = 0.76 Torr	$k_{P2}(T) = 2.90 \times 10^{-22} \times T^{3.09} \times \exp(782.5\ \mathrm{K}/T)$ (error fitting ~ 0.4%)
p = 7.6 Torr	$k_{P2}(T) = 2.93 \times 10^{-22} \times T^{3.09} \times \exp(781.5\ \mathrm{K}/T)$ (error fitting ~ 0.4%)
p = 76 Torr	$k_{P2}(T) = 2.79 \times 10^{-22} \times T^{3.09} \times \exp(784.3\ \mathrm{K}/T)$ (error fitting ~ 0.4%)
p = 760 Torr	$k_{P2}(T) = 3.17 \times 10^{-22} \times T^{3.08} \times \exp(774.4\ \mathrm{K}/T)$ (error fitting ~ 0.4%)
p = 7600 Torr	$k_{P2}(T) = 2.94 \times 10^{-22} \times T^{3.08} \times \exp(783.0\ \mathrm{K}/T)$ (error fitting ~ 0.4%)
p = 76,000 Torr	$k_{P2}(T) = 3.00 \times 10^{-22} \times T^{3.08} \times \exp(778.3\ \mathrm{K}/T)$ (error fitting ~ 0.4%)
2MTHF + OH → P3 + H_2O	
p = 0.76 Torr	$k_{P3}(T) = 1.20 \times 10^{-22} \times T^{3.18} \times \exp(818.3\ \mathrm{K}/T)$ (error fitting ~ 0.5%)
p = 7.6 Torr	$k_{P3}(T) = 1.26 \times 10^{-22} \times T^{3.18} \times \exp(813.4\ \mathrm{K}/T)$ (error fitting ~ 0.5%)
p = 76 Torr	$k_{P3}(T) = 1.18 \times 10^{-22} \times T^{3.19} \times \exp(818.1\ \mathrm{K}/T)$ (error fitting ~ 0.4%)
p = 760 Torr	$k_{P3}(T) = 1.23 \times 10^{-22} \times T^{3.18} \times \exp(815.6\ \mathrm{K}/T)$ (error fitting ~ 0.4%)
p = 7600 Torr	$k_{P3}(T) = 1.16 \times 10^{-22} \times T^{3.19} \times \exp(820.2\ \mathrm{K}/T)$ (error fitting ~ 0.4%)
p = 76,000 Torr	$k_{P3}(T) = 1.17 \times 10^{-22} \times T^{3.19} \times \exp(817.6\ \mathrm{K}/T)$ (error fitting ~ 0.4%)
2MTHF + OH → P4 + H_2O	
p = 0.76 Torr	$k_{P4}(T) = 3.47 \times 10^{-24} \times T^{3.61} \times \exp(1953.3\ \mathrm{K}/T)$ (error fitting ~ 3.6%)
p = 7.6 Torr	$k_{P4}(T) = 3.43 \times 10^{-24} \times T^{3.61} \times \exp(1955.0\ \mathrm{K}/T)$ (error fitting ~ 3.6%)
p = 76 Torr	$k_{P4}(T) = 3.33 \times 10^{-24} \times T^{3.61} \times \exp(1957.7\ \mathrm{K}/T)$ (error fitting ~ 3.6%)
p = 760 Torr	$k_{P4}(T) = 2.86 \times 10^{-24} \times T^{3.63} \times \exp(1974.0\ \mathrm{K}/T)$ (error fitting ~ 3.6%)
p = 7600 Torr	$k_{P4}(T) = 2.19 \times 10^{-24} \times T^{3.66} \times \exp(2013.1\ \mathrm{K}/T)$ (error fitting ~ 3.7%)
p = 76,000 Torr	$k_{P4}(T) = 1.80 \times 10^{-23} \times T^{3.39} \times \exp(1848.4\ \mathrm{K}/T)$ (error fitting ~ 6.0%)
2MTHF + OH → P5 + H_2O	
p = 0.76 Torr	$k_{P5}(T) = 1.31 \times 10^{-24} \times T^{3.95} \times \exp(966.8\ \mathrm{K}/T)$ (error fitting ~ 0.8%)
p = 7.6 Torr	$k_{P5}(T) = 1.24 \times 10^{-24} \times T^{3.96} \times \exp(969.2\ \mathrm{K}/T)$ (error fitting ~ 0.7%)
p = 76 Torr	$k_{P5}(T) = 1.33 \times 10^{-24} \times T^{3.95} \times \exp(966.1\ \mathrm{K}/T)$ (error fitting ~ 0.8%)
p = 760 Torr	$k_{P5}(T) = 1.33 \times 10^{-24} \times T^{3.95} \times \exp(964.7\ \mathrm{K}/T)$ (error fitting ~ 0.8%)
p = 7600 Torr	$k_{P5}(T) = 1.31 \times 10^{-24} \times T^{3.95} \times \exp(966.6\ \mathrm{K}/T)$ (error fitting ~ 0.8%)
p = 76,000 Torr	$k_{P5}(T) = 1.33 \times 10^{-24} \times T^{3.95} \times \exp(962.8\ \mathrm{K}/T)$ (error fitting ~ 0.7%)

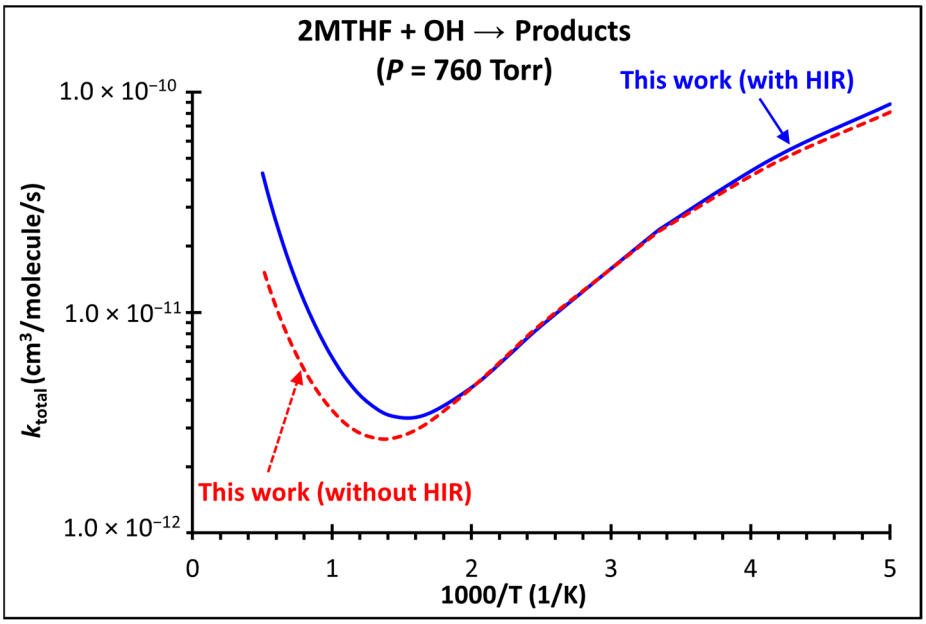

Figure 8. The impact of hindered internal rotation (HIR) treatment in the predicted values of the total rate coefficients, k_{tot}, for the reaction 2MTHF + OH → products.

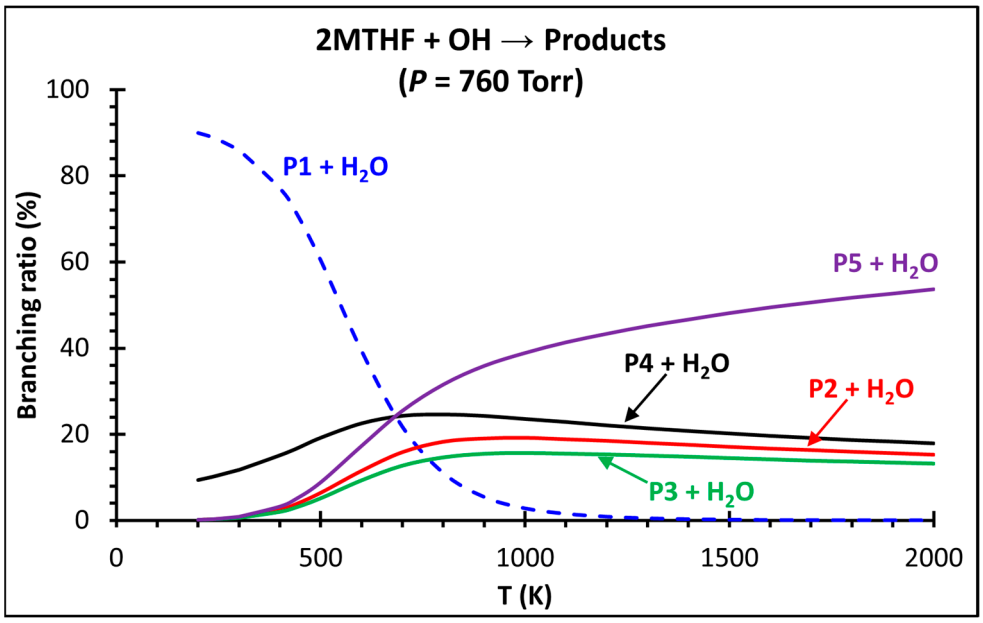

Figure 9. Temperature dependence of the product branching ratios for the reaction of 2MTHF + OH → products at p = 760 Torr. See Figure 3 for the species notations.

***k*(*T*, *p*) Comparison**. Figure 10 compares our computed rate coefficients with the experimental values at 760 Torr from different groups [16–18]. The quality of our computed rate coefficients for the OH + 2MTFH is nicely illustrated. The experimental values reported by Illés et al. [18] and Wallington et al. [16] for T = 240–400 K and p ~ 760 Torr showed a remarkable agreement. For example, our rate coefficient of 2.2 × 10^{-11} cm^3/molecule/s agrees well with the reports from Illés et al. [18] of 2.5 × 10^{-11} cm^3/molecule/s and Wallington et al. [16] of 2.2 × 10^{-11} cm^3/molecule/s at 298 K and 760 Torr. Within the reported uncertainties, our theoretical rate coefficients nicely captured the negative T-dependence of the rate coefficients exhibited by the experimental data (see Figure 10). In addition, our room temperature value showed an excellent agreement with the earlier

report of Illés et al. [17], who utilized the relative rate/gas chromatography technique (RR-GC) to measure the rate coefficient for OH + 2MTHF. However, their rate coefficient derived from the discharge flow technique (DF-RF) showed a large deviation (see Figure 10). Unfortunately, no experimental data are available at high temperatures for a reasonable comparison. The existing kinetic model of 2MTHF from Tripathi et al. [11] uses the total rate coefficients for OH + 2MTHF that are ~3 times higher than the calculated values in this work. Note that Tripathi et al. [11] used the reaction rate analogy to develop the oxidation kinetic model of 2MTHF. For the ring hydrogen abstraction reactions, the authors adopted the rate coefficients from the kinetic model of Tran et al. [89] for the OH + tetrahydrofuran reaction. For the methyl hydrogen abstraction of 2MTHF, they utilized the optimized rate coefficients of the OH + alkanes reactions [90], increasing the barrier height by 2 kcal/mol. The performance of the existing literature kinetic model with the updates of the theoretical site-specific rate coefficients for OH + 2MTHF from this work will be presented below. Our theoretically derived rate coefficients, $k(T, p)$, are listed in Tables 2 and 3.

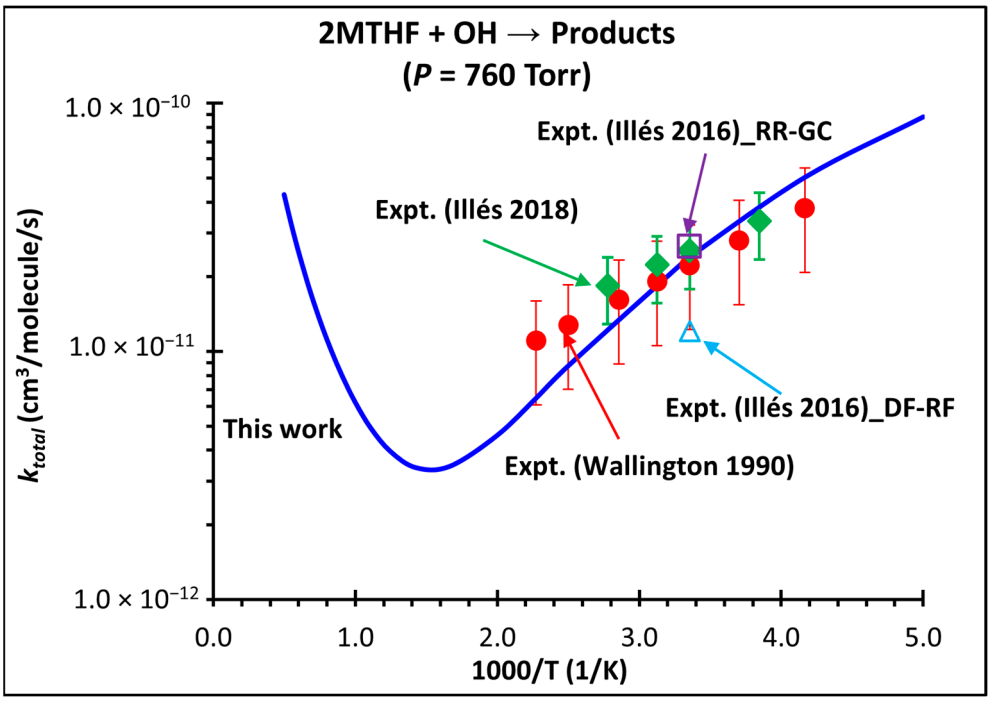

Figure 10. Comparison between the T-dependent theoretical (this work) and experimental (literature) rate coefficients at p = 760 Torr for 2MTHF + OH → products. Experimental data are from the works of Wallington et al. ("Expt. (Wallington 1990)" [16]); Illés et al. ("Expt. (Illés 2016)" [17] and "Expt. (Illés 2018)" [18]). "RR-GC" and "DF-RF" denote the experimental techniques of the relative rate and discharge flow.

3.4. Kinetic Modeling Implications

Figure 11 shows the integrated mass flux analysis based on C-atom for fuel 2MTHF consumption by various combustion species. The analysis was performed for a representative case of 760 K, 40 bar, and ϕ = 1.0. Figure 11a shows the branching of various 2MTHFyl radicals based on Tripathi et al. [11] kinetic models for 2MTHF. In contrast, Figure 11b displays the results after implementing the theoretical rate coefficients for the 2MTHF + OH and 2MTHF + HO_2 reactions from this work and Chakravarty and Fernandes [14], respectively. In Figure 11, the reactive species are given in the order of importance for the hydrogen abstraction reactions of 2MTHF. For example, OH, O, H signifies that the OH radical had the highest role followed by O and H atoms producing β- or γ-2MTHFyl radicals. Detailed kinetic modeling is beyond the scope of the current study. Therefore, we intend to illustrate how the radical product branching is affected by the incorporation

of the newly derived rate coefficients from this study in the existing model of Tripathi et al. [11]. As can be seen in Figure 11, the newly derived rate coefficients had a significant effect on 2MTHFyl radical distribution. As stated earlier, low-temperature branching is not possible for α-2MTHFyl radical. On the contrary, δ-2MTHFyl radical shows active low-temperature branching, expediting the oxidation kinetics of 2MTHF. The updated model significantly altered the product branching of α-2MTHFyl and δ-2MTHFyl radicals, e.g., 23% vs. 38% and 45% vs. 26% for α-2MTHFyl and δ-2MTHFyl radicals, respectively. According to Tripathi et al.'s model, only 1% of 2MTHF leads to forming β'-2MTHFyl radical. On the contrary, the updated model predicts as large as 15% of β'-2MTHFyl radical. Another noticeable difference was the participation of HO_2 radical reactions to deplete 2MTHF. Unlike the updated model, Tripathi et al.'s [11] model barely predicted the role of HO_2 reactions forming 2MTHFyl radicals at low temperatures (<1%). In conclusion, the updated kinetic model observed a significant difference in the flux analysis.

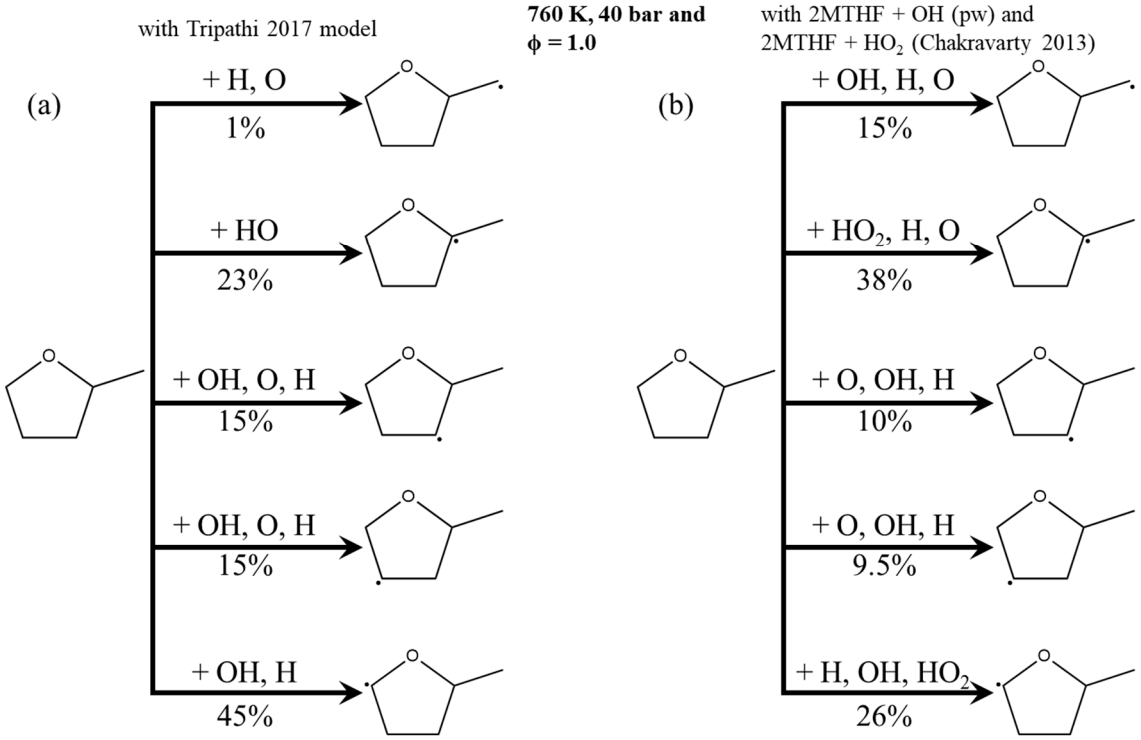

Figure 11. Integrated mass flux analysis based on C-atom of fuel (2MTHF) consumption for 2MTHF/air mixture at 760 K, 40 bar, and ϕ = 1.0. (**a**) using Tripathi et al.'s [11] models (**b**) updated Tripathi et al. [11] 2017 model by implementing our theoretical rate coefficients for the 2MTHF + OH reaction and the theoretical rate coefficients for the 2MTHF + HO_2 reaction from Chakravarty and Fernandes [14].

The effect of newly derived rate coefficients for OH + 2MTHF → products in the predictions of ignition delay times (IDTs) is further illustrated in Figure 12. As can be seen, the hydrogen abstraction reactions of 2MTHF by important combustion radicals/atoms species during the initial oxidation step of 2MTHF significantly influenced the predictive capabilities of the kinetic models. For accurate modeling of the combustion behavior of 2MTHF, the knowledge of the branching fractions of various abstraction reactions in the initial steps is critical. We demonstrated this fact with different scenarios, as discussed below.

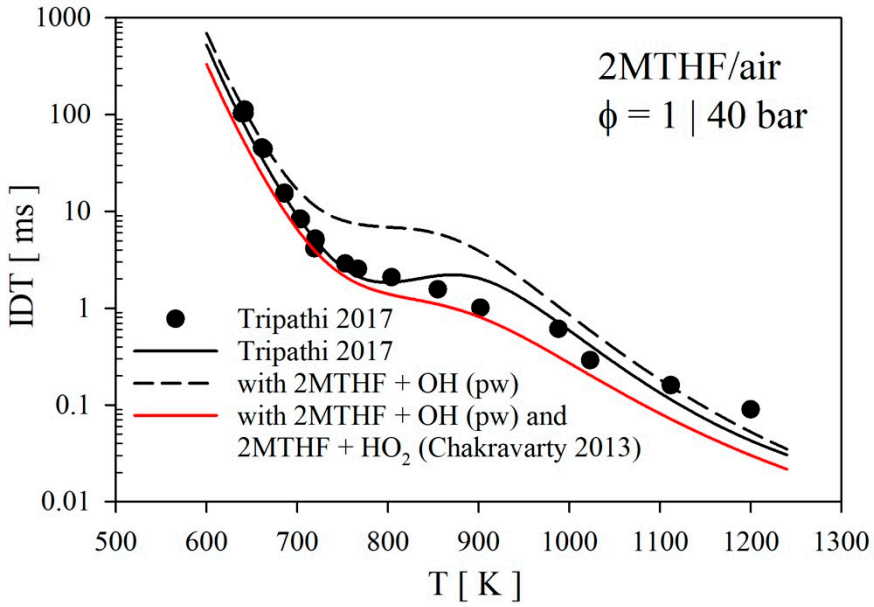

Figure 12. Effects of updated rate coefficients for OH/HO_2 + 2MTHF → products on the prediction of the ignition delay times of 2MTHF/air mixtures at 40 bar and ϕ = 1.0. The experimental data, together with the previous simulation results, are taken from the work by Tripathi et al. [11]. In the updated kinetic model, the rate coefficients for OH + 2MTHF → products and HO_2 + 2MTHF → products are taken from this work and Chakravarty and Fernandes [14], respectively. In figure legends, "pw" stands for present work.

With our rate coefficients, the model overpredicted the experimentally measured IDTs, particularly around the NTC regime. This behavior was not surprising because our theoretical rate coefficients for OH + 2MTHF → products were slower than those used in Tripathi et al.'s [11] models. Again, note that Tripathi et al. [11] used rate rules to assign the site-specific rate coefficients for the OH + 2MTHF reaction. More importantly, they did not use the theoretical rate coefficients for HO_2 + 2MTHF from Chakravarty and Fernandes [14], citing that their model severely underpredicted their experimental IDT data when the rate coefficients from Chakravarty and Fernandes [14] were used. However, the updated model performed remarkably well, capturing the experimental data with our rate coefficients for OH + 2MTHF and HO_2 + 2MTHF rate coefficients from Chakravarty and Fernandes [14] (see Figure 12). Unlike the original Tripathi et al. [11] model, the updated model predicted a less severe NTC behavior as indicated by the experimental data. We observed a similar behavior of the modeling performance in capturing the IDT behavior of 2MTHF oxidation at 20 bar and ϕ = 1.0 (see Figure S4 of SI).

Figure 13 illustrates the influence of the newly derived rate coefficients for OH + 2MTHF → products in predicting the laminar flame speed (LFS) of 2MTHF/air mixtures. The LFS data were taken from Wang et al. [91]. The solid lines represent the model predictions from Wang et al. [91]. We took Wang et al.'s [91] kinetic model and incorporated our rate coefficients for OH +2MTHF → products. As seen, the updated kinetic parameters for OH + 2MTHF → products influenced the LFS modeling predictions of 2MTHF/air mixtures. The updated model overpredicted the LFS on the lean side, whereas it captured the LFS better on the rich side. Building robust kinetic modeling to capture the various experimental targets over a wide range of conditions is beyond the scope of this work.

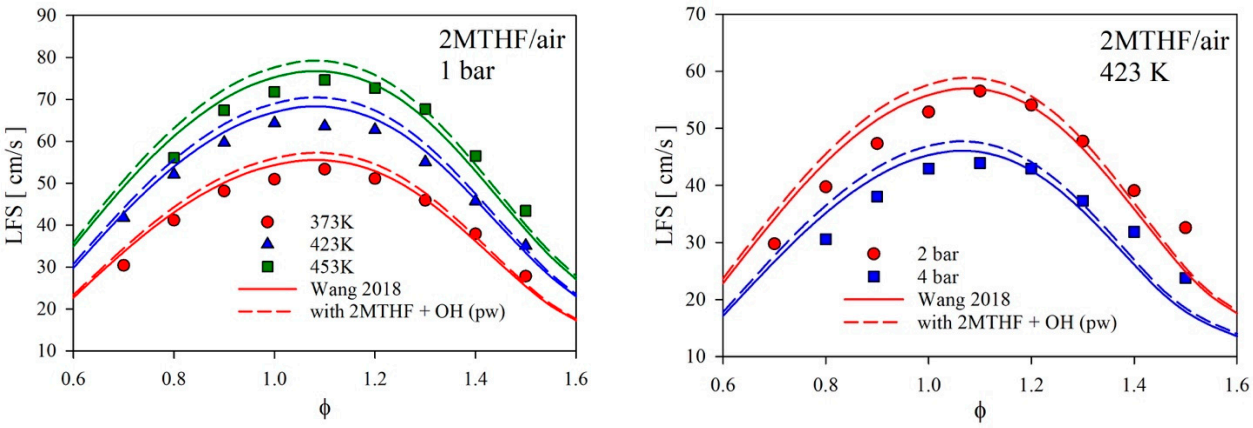

Figure 13. Effects of updated rate coefficients for OH/HO2 + 2MTHF → products on predicting the laminar flame speed of 2MTHF/air mixtures: (**a**) at 1 bar and 373, 423 & 453 K (**b**) at 423 K and 2 & 4 bar. In the updated kinetic model, the rate coefficients for OH + 2MTHF → products and HO_2 + 2MTHF → products were taken from this work and Chakravarty and Fernandes [14], respectively. The ex-perimental data were taken from Wang et al. [91]. Solid and broken lines represent the LFS pre-dictions from Wang et al. [91] and the updated kinetic model from this work.

4. Conclusions

The kinetics of OH radical reaction with 2-methyl tetrahydrofuran was theoretically investigated using ab-initio/RRKM-ME methods. The potential energy surface was mapped out at the CCSD(T)/cc-pVTZ//M06-2X/aug-cc-pVTZ level of theory. Some key points are summarized below:

1. The presence of heteroatom "O" weakened the adjacent C-H bond with the calculated bond dissociation energies in the order CH_2-H (~93) > C_β-H ≈ C_γ-H (~98) > C_δ-H (~94) > C_α-H (~93), in the unit of kcal/mol.
2. Our isodesmic values based on CBS-QB3 and W1U model chemistries for the heat of formation of various species (reactants and products) showed excellent agreement with the literature data.
3. The reaction of OH radicals with 2MTHF occurred via multiple steps in an overall exothermic process, and pre-reaction and post-reaction complexes existed at the entrance and exit channels.
4. The reaction displayed complex U-shaped kinetics. Interestingly, pressure dependence was observed at low temperatures, highlighting the importance of the pre-reaction complex in the proper RRKM-ME treatment of the OH + 2MTHF system. At T > 500 K, no discernible p-dependence was observed. It indicates that RC cannot be stabilized by pressure at high temperatures, even at extremely high pressures.
5. The **P1** + H_2O channel dominates at low temperatures (~80% at 200 K and 760 Torr). Since the transition state for the **P1** + H_2O channel was submerged below the reactants' energy, $k(T, p)$ showed a negative T-dependence for this channel. Above 700 K, the **P5** + H_2O channel was dominant (~60% at 2000 K and 760 Torr).
6. Our theoretical rate coefficients were in excellent agreement with experimental data, especially nicely capturing the experimental trend for the negative T-dependence of the reaction reported by Wallington et al. [16] and by Illés et al. [18].
7. The updated kinetic model with the newly derived rate coefficients from this work showed remarkable performance capturing the ignition delay times behavior of 2MTHF at low temperatures. The weak NTC behavior was predicted well with the updated kinetic model.

Supplementary Materials: The following supporting information can be downloaded at: https://www.mdpi.com/article/10.3390/en16093730/s1. Table S1: Optimized geometries, electronic energies at 0 K ($E_{elec}^{0\ K}$), zero-point energy (ZPE) corrections and harmonic wavenumbers of the species involved with the lowest-energy conformer of a given species, calculated at CCSD(T)/cc-pVTZ//M06-2X/aug-cc-pVTZ level of theory for the title reaction; Table S2: T1 diagnostics for the species involved in 2MTHF + OH reaction calculated at CCSD(T)/cc-pVTZ based on the M06-2X/aug-cc-pVTZ geometries; Table S3: Calculated global rate constants, ktot, of the 2MTHF + OH → products over the range of temperature 200–2000 K at different pressures, including the HIR treatments and Eckart quantum tunneling effects. Units are in cm^3/molecule/s. The $k_{tot}(T, P)$ at different pressures are fitted as the double-modified Arrhenius formats; Table S4: The calculated Eckart tunneling factor via tight transition state channels over the wide range of temperature 200–2000 K; Table S5: Calculated overall rate constants, k_{tot}, of the 2MTHF + OH → products over the range of temperature 200–2000 K at P = 760 Torr with and without HIR treatments based on M06-2X/aug-cc-pVTZ level of theory. Units are in cm^3/molecule/s; Table S6: Calculated NASA coefficients for the thermodynamic properties of various species in the reaction of OH radicals with 2MTHF; Figure S1: M06-2X/aug-cc-pVTZ optimized geometries for the species involved in the title reaction. All structures were obtained for the lowest-energy conformer of a given species. Bond lengths and bond angles are in Å and degree (°), respectively; Figure S2: Hindrance potentials for the species involved in the 2MTHF + OH reaction, calculated at M06-2X/cc-pVDZ level of theory; Figure S3: Effects of updated rate coefficients for OH/HO_2 + 2MTHF → products on the prediction of the ignition delay times of 2MTHF/air mixtures at 20 bar and ϕ = 0.5. The experimental data are taken from Tripathi et al. The comparison of the various scenarios for the performance of the kinetic model is shown. The red line shows the performance of the updated kinetic model from this work with the rate coefficients for OH + 2MTHF → products (this work) and HO_2 + 2MTHF → products (Chakravarty and Fernandes); Figure S4: Optimized TSs and corresponding RCs obtained at M06-2X/aug-cc-pVTZ level; Figure S5: Simplified PES for the formation of RCs from 2MTHF and OH radical (+ZPE, 0 K) calculated at CCSD(T)/cc-pVTZ//M06-2X/aug-cc-pVTZ; Figure S6: Comparison of the computed global rate constants (2MTHF + OH → products) using one-RC (RCa) and two-RC models (RCa & RCb) at P = 760 Torr. Refs. [11,14,26,27,92] are cited in the Supplementary Materials.

Author Contributions: Conceptualization, T.V.-T.M. and L.K.H.; Methodology, K.P.S. and B.R.G.; Software, T.V.-T.M. and L.K.H.; Formal analysis, T.Q.B.; Investigation, T.V.-T.M., N.T.A.N., P.T.Q., F.M., B.R.G. and L.K.H.; Data curation, K.P.S.; Writing—original draft, T.V.-T.M., T.Q.B., P.T.Q. and K.P.S.; Writing—review & editing, N.T.A.N., F.M., B.R.G. and L.K.H.; Visualization, T.V.-T.M.; Supervision, B.R.G. and L.K.H.; Project administration, L.K.H.; Funding acquisition, L.K.H. All authors have read and agreed to the published version of the manuscript.

Funding: This work was funded by Vietnam National Foundation for Science and Technology Development (NAFOSTED) under grant number 104.06-2020.45.

Data Availability Statement: The data presented in this study are available in this article and Supplementary Materials.

Acknowledgments: We want to thank Tuyn Phan and Tri Pham (ICST) for their technical assistance.

Conflicts of Interest: The authors declare no conflict of interest.

References

1. Rotavera, B.; Taatjes, C.A. Influence of functional groups on low-temperature combustion chemistry of biofuels. *Prog. Energy Combust. Sci.* **2021**, *86*, 100925. [CrossRef]
2. Tran, L.-S.; Herbinet, O.; Carstensen, H.-H.; Battin-Leclerc, F. Chemical kinetics of cyclic ethers in combustion. *Prog. Energy Combust. Sci.* **2022**, *92*, 101019. [CrossRef]
3. Rudolph, T.W.; Thomas, J.J. NOx, NMHC and CO emissions from biomass derived gasoline extenders. *Biomass* **1988**, *16*, 33–49. [CrossRef]
4. Alonso, D.M.; Bond, J.Q.; Dumesic, J.A. Catalytic conversion of biomass to biofuels. *Green Chem.* **2010**, *12*, 1493–1513. [CrossRef]
5. Janssen, A.J.; Kremer, F.W.; Baron, J.H.; Muether, M.; Pischinger, S.; Klankermayer, J. Tailor-Made Fuels from Biomass for Homogeneous Low-Temperature Diesel Combustion. *Energy Fuels* **2011**, *25*, 4734–4744. [CrossRef]
6. Tuan Hoang, A.; Viet Pham, V. 2-Methylfuran (MF) as a potential biofuel: A thorough review on the production pathway from biomass, combustion progress, and application in engines. *Renew. Sust. Energ. Rev.* **2021**, *148*, 111265. [CrossRef]

7. Mehdi, H.; Fábos, V.; Tuba, R.; Bodor, A.; Mika, L.T.; Horváth, I.T. Integration of Homogeneous and Heterogeneous Catalytic Processes for a Multi-step Conversion of Biomass: From Sucrose to Levulinic Acid, γ-Valerolactone, 1,4-Pentanediol, 2-Methyltetrahydrofuran, and Alkanes. *Top. Catal.* **2008**, *48*, 49–54. [CrossRef]
8. Wright, W.R.; Palkovits, R. Development of heterogeneous catalysts for the conversion of levulinic acid to gamma-valerolactone. *ChemSusChem* **2012**, *5*, 1657–1667. [CrossRef]
9. Alonso, D.M.; Wettstein, S.G.; Dumesic, J.A. Gamma-valerolactone, a sustainable platform molecule derived from lignocellulosic biomass. *Green Chem.* **2013**, *15*, 584–595. [CrossRef]
10. Sims, R.E.; Mabee, W.; Saddler, J.N.; Taylor, M. An overview of second generation biofuel technologies. *Bioresour. Technol.* **2010**, *101*, 1570–1580. [CrossRef]
11. Tripathi, R.; Lee, C.; Fernandes, R.X.; Olivier, H.; Curran, H.J.; Mani Sarathy, S.; Pitsch, H. Ignition characteristics of 2-methyltetrahydrofuran: An experimental and kinetic study. *Proc. Combust. Inst.* **2017**, *36*, 587–595. [CrossRef]
12. Fenard, Y.; Boumehdi, M.A.; Vanhove, G. Experimental and kinetic modeling study of 2-methyltetrahydrofuran oxidation under engine-relevant conditions. *Combust. Flame* **2017**, *178*, 168–181. [CrossRef]
13. Moshammer, K.; Vranckx, S.; Chakravarty, H.K.; Parab, P.; Fernandes, R.X.; Kohse-Höinghaus, K. An experimental and kinetic modeling study of 2-methyltetrahydrofuran flames. *Combust. Flame* **2013**, *160*, 2729–2743. [CrossRef]
14. Chakravarty, H.K.; Fernandes, R.X. Reaction kinetics of hydrogen abstraction reactions by hydroperoxyl radical from 2-methyltetrahydrofuran and 2,5-dimethyltetrahydrofuran. *J. Phys. Chem. A* **2013**, *117*, 5028–5041. [CrossRef]
15. Pitz, W.J.; Naik, C.V.; Mhaoldúin, T.N.; Westbrook, C.K.; Curran, H.J.; Orme, J.P.; Simmie, J.M. Modeling and experimental investigation of methylcyclohexane ignition in a rapid compression machine. *Proc. Combust. Inst.* **2007**, *31*, 267–275. [CrossRef]
16. Wallington, T.J.; Siegl, W.O.; Liu, R.; Zhang, Z.; Huie, R.E.; Kurylo, M.J. The atmospheric reactivity of α-methyltetrahydrofuran. *Environ. Sci. Technol.* **1990**, *24*, 1596–1599. [CrossRef]
17. Illés, Á.; Farkas, M.; Zügner, G.L.; Novodárszki, G.; Mihályi, M.; Dóbé, S. Direct and relative rate coefficients for the gas-phase reaction of OH radicals with 2-methyltetrahydrofuran at room temperature. *React. Kinet. Mech. Catal.* **2016**, *119*, 5–18. [CrossRef]
18. Illés, Á.; Nagy, M.; Novodárszki, G.; Mihályi, M.; Dóbé, S. Temperature dependent rate coefficient for the reaction of oh radicals with 2-methyltetrahydrofuran in gas phase. *Oxid. Commun.* **2018**, *41*, 189–194.
19. Zhao, Y.; Truhlar, D.G. Density functionals with broad applicability in chemistry. *Acc. Chem. Res.* **2008**, *41*, 157–167. [CrossRef]
20. Zhao, Y.; Truhlar, D.G. The M06 suite of density functionals for main group thermochemistry, thermochemical kinetics, noncovalent interactions, excited states, and transition elements: Two new functionals and systematic testing of four M06-class functionals and 12 other functionals. *Theor. Chem. Acc.* **2007**, *120*, 215–241. [CrossRef]
21. Frisch, M.J.; Trucks, G.W.; Schlegel, H.B.; Scuseria, G.E.; Robb, M.A.; Cheeseman, J.R.; Scalmani, G.; Barone, V.; Mennucci, B.; Petersson, G.A.; et al. *Gaussian 09, Revision A.1*; Gaussian, Inc.: Wallingford, CT, USA, 2009.
22. Alecu, I.M.; Zheng, J.; Zhao, Y.; Truhlar, D.G. Computational Thermochemistry: Scale Factor Databases and Scale Factors for Vibrational Frequencies Obtained from Electronic Model Chemistries. *J. Chem. Theory Comput.* **2010**, *6*, 2872–2887. [CrossRef] [PubMed]
23. Gonzalez, C.; Schlegel, H.B. An improved algorithm for reaction path following. *J. Chem. Phys.* **1989**, *90*, 2154–2161. [CrossRef]
24. Gonzalez, C.; Schlegel, H.B. Reaction path following in mass-weighted internal coordinates. *J. Phys. Chem.* **1990**, *94*, 5523–5527. [CrossRef]
25. Huber, K.-P. *Molecular Spectra and Molecular Structure: IV. Constants of Diatomic Molecules*; Springer Science & Business Media: New York, NY, USA, 2013.
26. Hoy, A.R.; Bunker, P.R. A precise solution of the rotation bending Schrödinger equation for a triatomic molecule with application to the water molecule. *J. Mol. Spectrosc.* **1979**, *74*, 1–8. [CrossRef]
27. Huber, K.P.; Herzberg, G. *Molecular Spectra and Molecular Structure: IV. Constants of Diatomic Molecules*; Van Nostrand Reinhold Co.: Washington, DC, USA, 1979. [CrossRef]
28. Robinson, R.K.; Lindstedt, R.P. A comparative ab initio study of hydrogen abstraction from n-propyl benzene. *Combust. Flame* **2013**, *160*, 2642–2653. [CrossRef]
29. Yin, G.; Hu, E.; Zhou, M.; Zhan, H.; Huang, Z. Kinetic Study on the Isomerization and Decomposition of the Alkenyl Radicals of 2,4,4-Trimethyl-1-pentene. *Energy Fuels* **2020**, *34*, 14757–14767. [CrossRef]
30. Mai, T.V.; Huynh, L.K. Comment on "Atmospheric oxidation reactions of imidazole initiated by hydroxyl radicals: Kinetics and mechanism of reactions and atmospheric implications" by Safaei et al., *Phys. Chem. Chem. Phys.*, **2019**, *21*, 8445. *Phys. Chem. Chem. Phys.* **2019**, *21*, 21162–21165. [CrossRef]
31. Mai, T.V.T.; Nguyen, H.T.; Huynh, L.K. Ab Initio Kinetic Mechanism of OH-Initiated Atmospheric Oxidation of Pyrrole. *Chemosphere* **2020**, *263*, 127850. [CrossRef]
32. Mai, T.V.T.; Huynh, L.K. Detailed Kinetics of Hydrogen Abstraction from *trans*-Decalin by OH Radicals: The Role of Hindered Internal Rotation Treatment. *Phys. Chem. Chem. Phys.* **2020**, *22*, 25740–25746. [CrossRef]
33. Mai, T.V.T.; Huynh, L.K. Comment on "Atmospheric chemistry of oxazole: The mechanism and kinetic studies on oxidation reaction initiated by OH radicals" by A. Shiroudi, M.A. Abdel-Rahman, A.M. El-Nahas and M. Altarawneh, *New J. Chem.*, **2021**, *45*, 2237. *New J. Chem.* **2021**, *45*, 13644–13648. [CrossRef]
34. Mai, T.V.-T.; Nguyen, T.T.-D.; Nguyen, H.T.; Nguyen, T.T.; Huynh, L.K. New Mechanistic Insights into Atmospheric Oxidation of Aniline Initiated by OH Radicals. *Environ. Sci. Technol.* **2021**, *55*, 7858–7868. [CrossRef] [PubMed]

35. Giri, B.R.; Mai, T.V.T.; Assali, M.; Nguyen, T.T.; Nguyen, H.T.; Szori, M.; Huynh, L.K.; Fittschen, C.; Farooq, A. Reaction kinetics of 1,4-cyclohexadienes with OH radicals: An experimental and theoretical study. *Phys. Chem. Chem. Phys.* **2022**, *24*, 7836–7847. [CrossRef] [PubMed]
36. Mai, T.V.T.; Nguyen, H.D.; Nguyen, P.-D.; Nguyen, H.T.; Na, O.M.; Le, T.H.M.; Huynh, L.K. Ab initio kinetics of OH-initiated oxidation of cyclopentadiene. *Fuel* **2022**, *317*, 123305. [CrossRef]
37. Giri, B.R.; Mai, T.V.-T.; Nguyen, T.T.-D.; Szőri, M.; Huynh, L.K.; Farooq, A. Kinetic Insights into the Reaction of Hydroxyl Radicals with 1,4-Pentadiene: A Combined Experimental and Theoretical Study. *Combust. Flame* **2022**, *241*, 112153. [CrossRef]
38. Xie, H.B.; Li, C.; He, N.; Wang, C.; Zhang, S.; Chen, J. Atmospheric chemical reactions of monoethanolamine initiated by OH radical: Mechanistic and kinetic study. *Environ. Sci. Technol.* **2014**, *48*, 1700–1706. [CrossRef]
39. Arathala, P.; Musah, R.A. Computational Study Investigating the Atmospheric Oxidation Mechanism and Kinetics of Dipropyl Thiosulfinate Initiated by OH Radicals, and the Fate of Propanethiyl Radical. *J. Phys. Chem. A* **2020**, *124*, 8292–8304. [CrossRef]
40. Purvis, G.D.; Bartlett, R.J. A full coupled-cluster singles and doubles model: The inclusion of disconnected triples. *J. Chem. Phys.* **1982**, *76*, 1910–1918. [CrossRef]
41. Scuseria, G.E.; Janssen, C.L.; Schaefer, H.F. An efficient reformulation of the closed-shell coupled cluster single and double excitation (CCSD) equations. *J. Chem. Phys.* **1988**, *89*, 7382–7387. [CrossRef]
42. Scuseria, G.E.; Schaefer, H.F. Is coupled cluster singles and doubles (CCSD) more computationally intensive than quadratic configuration interaction (QCISD)? *J. Chem. Phys.* **1989**, *90*, 3700–3703. [CrossRef]
43. Lee, T.J.; Taylor, P.R. A diagnostic for determining the quality of single-reference electron correlation methods. *Int. J. Quantum Chem.* **1989**, *36*, 199–207. [CrossRef]
44. Jayatilaka, D.; Lee, T.J. Open-shell coupled-cluster theory. *J. Chem. Phys.* **1993**, *98*, 9734–9747. [CrossRef]
45. Gillespie, D.T. A general method for numerically simulating the stochastic time evolution of coupled chemical reactions. *J. Comput. Phys.* **1976**, *22*, 403–434. [CrossRef]
46. Gillespie, D.T.; Hellander, A.; Petzold, L.R. Perspective: Stochastic algorithms for chemical kinetics. *J. Chem. Phys.* **2013**, *138*, 170901–170914. [CrossRef] [PubMed]
47. Duong, M.V.; Nguyen, H.T.; Truong, N.; Le, T.N.M.; Huynh, L.K. Multi-Species Multi-Channel (MSMC): An Ab Initio-based Parallel Thermodynamic and Kinetic Code for Complex Chemical Systems. *Int. J. Chem. Kinet.* **2015**, *47*, 564–575. [CrossRef]
48. Duong, M.V.; Nguyen, H.T.; Mai, T.V.; Huynh, L.K. Global minimum profile error (GMPE)—A least-squares-based approach for extracting macroscopic rate coefficients for complex gas-phase chemical reactions. *Phys. Chem. Chem. Phys.* **2018**, *20*, 1231–1239. [CrossRef]
49. Mai, T.V.T.; Duong, M.V.; Le, X.T.; Huynh, L.K.; Ratkiewicz, A. Direct ab initio dynamics calculations of thermal rate constants for the $CH_4 + O_2 = CH_3 + HO_2$ reaction. *Struct. Chem.* **2014**, *25*, 1495–1503. [CrossRef]
50. Le, T.H.M.; Do, S.T.; Huynh, L.K. Algorithm for auto-generation of hindered internal rotation parameters for complex chemical systems. *Comput. Theor. Chem.* **2017**, *1100*, 61–69. [CrossRef]
51. Le, T.H.M.; Tran, T.T.; Huynh, L.K. Identification of hindered internal rotational mode for complex chemical species: A data mining approach with multivariate logistic regression model. *Chemom. Intell. Lab. Syst.* **2018**, *172*, 10–16. [CrossRef]
52. Beyer, T.; Swinehart, D.F. Algorithm 448: Number of multiply-restricted partitions. *Commun. ACM* **1973**, *16*, 379. [CrossRef]
53. Cooley, J.W.; Tukey, J.W. An Algorithm for the Machine Calculation of Complex Fourier Series. *Math. Comput.* **1965**, *19*, 297–301. [CrossRef]
54. Eckart, C. The Penetration of a Potential Barrier by Electrons. *Phys. Rev.* **1930**, *35*, 1303–1309. [CrossRef]
55. Coxon, J.A.; Foster, S.C. Radial dependence of spin-orbit and Λ-doubling parameters in the X2Π ground state of hydroxyl. *J. Mol. Spectrosc.* **1982**, *91*, 243–254. [CrossRef]
56. Mai, T.V.T.; Huynh, L.K. The role of low-lying conformers and pressure effect in kinetic modeling of hydrogen abstraction of tertiary amyl methyl ether by OH radicals. *Fuel* **2020**, *260*, 116313. [CrossRef]
57. Mai, T.V.; Nguyen, H.T.; Huynh, L.K. Ab initio dynamics of hydrogen abstraction from N2H4 by OH radicals: An RRKM-based master equation study. *Phys. Chem. Chem. Phys.* **2019**, *21*, 23733–23741. [CrossRef]
58. Mai, T.V.T.; Nguyen, H.T.; Huynh, L.K. Atmospheric chemistry of the reaction between propylene carbonate and OH radical: An ab initio RRKM-based master equation study. *Chem. Phys. Lett.* **2020**, *739*, 137020. [CrossRef]
59. Mai, T.V.T.; Nguyen, H.T.; Huynh, L.K. Kinetics of hydrogen abstraction from CH3SH by OH radicals: An ab initio RRKM-based master equation study. *Atmos. Environ.* **2020**, *242*, 117833. [CrossRef]
60. Hippler, H. Collisional deactivation of vibrationally highly excited polyatomic molecules. II. Direct observations for excited toluene. *J. Chem. Phys.* **1983**, *78*, 6709. [CrossRef]
61. Somers, K.P.; Simmie, J.M.; Metcalfe, W.K.; Curran, H.J. The pyrolysis of 2-methylfuran: A quantum chemical, statistical rate theory and kinetic modelling study. *Phys. Chem. Chem. Phys.* **2014**, *16*, 5349–5367. [CrossRef]
62. Robertson, S.H.; Pilling, M.J.; Baulch, D.L.; Green, N.J.B. Fitting of pressure-dependent kinetic rate data by master equation/inverse Laplace transform analysis. *J. Phys. Chem.* **1995**, *99*, 13452–13460. [CrossRef]
63. Georgievskii, Y.; Klippenstein, S.J. Long-range transition state theory. *J. Chem. Phys.* **2005**, *122*, 194103–194117. [CrossRef]
64. Simmie, J.M. Kinetics and thermochemistry of 2,5-dimethyltetrahydrofuran and related oxolanes: Next next-generation biofuels. *J. Phys. Chem. A* **2012**, *116*, 4528–4538. [CrossRef] [PubMed]
65. Luo, Y.-R. *Comprehensive Handbook of Chemical Bond Energies*; CRC Press: Boca Raton, FL, USA, 2007. [CrossRef]

66. Montgomery, J.A., Jr.; Frisch, M.J.; Ochterski, J.W.; Petersson, G.A. A complete basis set model chemistry. VI. Use of density functional geometries and frequencies. *J. Chem. Phys.* **1999**, *110*, 2822–2827. [CrossRef]
67. Andersson, K.; Malmqvist, P.-A.K.; Roos, B.R.O. Second-order perturbation theory with a complete active space self-consistent field reference function. *J. Chem. Phys.* **1992**, *96*, 1218. [CrossRef]
68. Celani, P.; Werner, H.-J. Multireference perturbation theory for large restricted and selected active space reference wave functions. *J. Chem. Phys.* **2000**, *112*, 5546. [CrossRef]
69. Werner, H.-J. Third-order multireference perturbation theory The CASPT3 method. *Mol. Phys.* **1996**, *89*, 645–661. [CrossRef]
70. Auzmendi-Murua, I.; Charaya, S.; Bozzelli, J.W. Thermochemical properties of methyl-substituted cyclic alkyl ethers and radicals for oxiranes, oxetanes, and oxolanes: C-H bond dissociation enthalpy trends with ring size and ether site. *J. Phys. Chem. A* **2013**, *117*, 378–392. [CrossRef]
71. Wijaya, C.D.; Sumathi, R.; Green, W.H. Thermodynamic Properties and Kinetic Parameters for Cyclic Ether Formation from Hydroperoxyalkyl Radicals. *J. Phys. Chem. A* **2003**, *107*, 4908–4920. [CrossRef]
72. Goos, E.; Burcat, A.; Ruscic, B. *Extended Third Millennium Ideal Gas and Condensed Phase Thermochemical Database for Combustion with Updates from Active Thermochemical Tables*; Argonne National Laboratory: Lemont, IL, USA, 2010.
73. Chase, M.W., Jr. *NIST-JANAF Thermochemical Tables*, 4th ed.; American Institute of Physics: College Park, MD, USA, 1998; 1951p.
74. Ochterski, J.W. *Thermochemistry in Gaussian*; Gaussian Inc.: Pittsburgh, PA, USA, 2000.
75. Hehre, W.J.; Ditchfield, R.; Radom, L.; Pople, J.A. Molecular orbital theory of the electronic structure of organic compounds. V. Molecular theory of bond separation. *J. Am. Chem. Soc.* **1970**, *92*, 4796–4801. [CrossRef]
76. Ruscic, B.; Bross, D.H. *Active Thermochemical Tables (ATcT) Values Based on Ver. 1.122d of the Thermochemical Network*; Argonne National Laboratory: Lemont, IL, USA, 2018.
77. Pilcher, G.; Pell, A.S.; Coleman, D.J. Measurements of heats of combustion by flame calorimetry. Part 2.—Dimethyl ether, methyl ethyl ether, methyl n-propyl ether, methyl isopropyl ether. *Trans. Faraday Soc.* **1964**, *60*, 499–505. [CrossRef]
78. Good, W.D.; Smith, N.K. Enthalpies of combustion of toluene, benzene, cyclohexane, cyclohexene, methylcyclopentane, 1-methylcyclopentene, and n-hexane. *J. Chem. Eng. Data* **1969**, *14*, 102–106. [CrossRef]
79. Pittam, D.A.; Pilcher, G. Measurements of heats of combustion by flame calorimetry. Part 8.—Methane, ethane, propane, n-butane and 2-methylpropane. *J. Chem. Soc. Faraday Trans. Phys. Chem. Condens. Phases* **1972**, *68*, 2224–2229. [CrossRef]
80. Giri, B.R.; Khaled, F.; Szőri, M.; Viskolcz, B.; Farooq, A. An experimental and theoretical kinetic study of the reaction of OH radicals with tetrahydrofuran. *Proc. Combust. Inst.* **2016**, *36*, 143–150. [CrossRef]
81. Illés, Á.; Borbála Rózsa, Z.; Thangaraj, R.; Décsiné Gombos, E.; Dóbé, S.; Raj Giri, B.; Szőri, M. An experimental and theoretical kinetic study of the reactions of hydroxyl radicals with tetrahydrofuran and two deuterated tetrahydrofurans. *Chem. Phys. Lett.* **2021**, *776*, 138698. [CrossRef]
82. Khaled, F.; Giri, B.R.; Szori, M.; Mai, T.V.T.; Huynh, L.K.; Farooq, A. A combined high-temperature experimental and theoretical kinetic study of the reaction of dimethyl carbonate with OH radicals. *Phys. Chem. Chem. Phys.* **2017**, *19*, 7147–7157. [CrossRef] [PubMed]
83. Fan, C.; Wang, W.; Shi, B.; Chen, Y.; Wang, K.; Zhang, W.; Sun, Z.; Ge, M. A Combined Experimental and Theoretical Study on the Gas Phase Reaction of OH Radicals with Ethyl Propyl Ether. *J. Phys. Chem. A* **2020**, *124*, 721–730. [CrossRef]
84. Shannon, R.J.; Blitz, M.A.; Goddard, A.; Heard, D.E. Accelerated chemistry in the reaction between the hydroxyl radical and methanol at interstellar temperatures facilitated by tunnelling. *Nat. Chem.* **2013**, *5*, 745–749. [CrossRef]
85. Gao, L.G.; Zheng, J.; Fernandez-Ramos, A.; Truhlar, D.G.; Xu, X. Kinetics of the Methanol Reaction with OH at Interstellar, Atmospheric, and Combustion Temperatures. *J. Am. Chem. Soc.* **2018**, *140*, 2906–2918. [CrossRef]
86. Galano, A.; Raúl Alvarez-Idaboy, J. Chapter 12—Atmospheric Reactions of Oxygenated Volatile Organic Compounds + OH Radicals: Role of Hydrogen-Bonded Intermediates and Transition States. In *Advances in Quantum Chemistry*; Academic Press: Cambridge, MA, USA, 2008; Volume 55.
87. Arathala, P.; Tangtartharakul, C.B.; Sinha, A. Atmospheric Ring-Closure and Dehydration Reactions of 1,4-Hydroxycarbonyls in the Gas Phase: The Impact of Catalysts. *J. Phys. Chem. A* **2021**, *125*, 5963–5975. [CrossRef]
88. Liu, D.; Giri, B.R.; Mai, T.V.T.; Huynh, L.K.; Farooq, A. Reaction kinetics of OH radicals with 1,3,5-trimethyl benzene: An experimental and theoretical study. *Proc. Combust. Inst.* **2022**, *in press*. [CrossRef]
89. Tran, L.-S.; Verdicchio, M.; Monge, F.; Martin, R.C.; Bounaceur, R.; Sirjean, B.; Glaude, P.-A.; Alzueta, M.U.; Battin-Leclerc, F. An experimental and modeling study of the combustion of tetrahydrofuran. *Combust. Flame* **2015**, *162*, 1899–1918. [CrossRef]
90. Cai, L.; Pitsch, H.; Mohamed, S.Y.; Raman, V.; Bugler, J.; Curran, H.; Sarathy, S.M. Optimized reaction mechanism rate rules for ignition of normal alkanes. *Combust. Flame* **2016**, *173*, 468–482. [CrossRef]
91. Wang, X.; Fan, X.; Yang, K.; Wang, J.; Jiao, X.; Guo, Z. Laminar flame characteristics and chemical kinetics of 2-methyltetrahydrofuran and the effect of blending with isooctane. *Combust. Flame* **2018**, *191*, 213–225. [CrossRef]
92. Shimanouchi, T. Tables of Molecular Vibrational Frequencies, Consolidated Volume 1, NSRDS NBS-39. Available online: https://nvlpubs.nist.gov/nistpubs/Legacy/NSRDS/nbsnsrds39.pdf (accessed on 1 March 2022).